



HAL
open science

Investigation of magnetic hysteresis in biased Ta/Pt/Co/FeMn/Ta antidots: Influence of structural dimensions

Farid Fettar, Laurent Cagnon, David Barral, Patrice David, Loris Naudin, Florent Blondelle, Frédéric Gay

► To cite this version:

Farid Fettar, Laurent Cagnon, David Barral, Patrice David, Loris Naudin, et al.. Investigation of magnetic hysteresis in biased Ta/Pt/Co/FeMn/Ta antidots: Influence of structural dimensions. *Journal of Applied Physics*, 2024, 135 (1), pp.013903. 10.1063/5.0173469 . hal-04777248

HAL Id: hal-04777248


<https://hal.science/hal-04777248v1>

Submitted on 12 Nov 2024

HAL is a multi-disciplinary open access archive for the deposit and dissemination of scientific research documents, whether they are published or not. The documents may come from teaching and research institutions in France or abroad, or from public or private research centers.

L'archive ouverte pluridisciplinaire **HAL**, est destinée au dépôt et à la diffusion de documents scientifiques de niveau recherche, publiés ou non, émanant des établissements d'enseignement et de recherche français ou étrangers, des laboratoires publics ou privés.

AUTHOR QUERY FORM

	<p>Journal: J. Appl. Phys.</p> <p>Article Number: JAP23-AR-03521</p>	<p>Please provide your responses and any corrections by annotating this PDF and uploading it to AIP's eProof website as detailed in the Welcome email.</p>
---	---	--

Dear Author,

Below are the queries associated with your article; please answer all of these queries before sending the proof back to AIP.

Article checklist: In order to ensure greater accuracy, please check the following and make all necessary corrections before returning your proof.

1. Is the title of your article accurate and spelled correctly?
2. Please check affiliations including spelling, completeness, and correct linking to authors.
3. Did you remember to include acknowledgment of funding, if required, and is it accurate?

Location in article	Query / Remark: click on the Q link to navigate to the appropriate spot in the proof. There, insert your comments as a PDF annotation.
Q1	<p>Please check that the author names are in the proper order and spelled correctly. Also, please ensure that each author's given and surnames have been correctly identified (given names are highlighted in red and surnames appear in blue).</p>
	<p>Please confirm ORCID's are accurate. If you wish to add an ORCID for any author that does not have one, you may do so now. For more information on ORCID, see https://orcid.org/.</p> <p style="margin-left: 40px;"> F. Fettar–0009-0009-3811-6096 L. Cagnon–0000-0002-5023-9437 D. Barral P. David–0009-0004-3420-9504 L. Naudin–0009-0008-6109-9987 F. Blondelle–0009-0001-6994-9594 F. Gay–0000-0002-5322-1443 </p>
	<p>Please check and confirm the Funder(s) and Grant Reference Number(s) provided with your submission:</p> <p>Please add any additional funding sources not stated above:</p>

Thank you for your assistance.

Investigation of magnetic hysteresis in biased Ta/Pt/Co/FeMn/Ta antidots: Influence of structural dimensions

Cite as: J. Appl. Phys. 135, 000000 (2024); doi: 10.1063/5.0173469

Submitted: 22 August 2023 · Accepted: 11 December 2023 ·

Published Online: ■■ ■■ 2023



F. Fettar,^{a)} L. Cagnon, D. Barral, P. David, L. Naudin, F. Blondelle, and F. Gay

AFFILIATIONS

Institut Néel, Université Grenoble Alpes, F-38042 Grenoble, France

^{a)} Author to whom correspondence should be addressed: farid.fettar@neel.cnrs.fr

ABSTRACT

There exists a controversy in the literature concerning the values of coercive and bias fields in antidots magnetic structures formed by a hexagonal network of nanoholes. The coercive fields (H_C) and the exchange bias fields ($|H_{EXC}|$) for antidots (deposited on ultrathin anodic aluminum oxide, namely, AAO) are either increased or diminished by comparison with the same magnetic nanostructures grown on continuous substrates (namely, CML). We propose to elucidate these debates by showing the importance of the easy axis of the magnetization, the direction of the applied magnetic field, the thicknesses of the layers, and the 3D-topology of nanoholes, as well as the magnetic and thermal history of the magnetic measurements. Here, biased Ta(5 nm)/Pt(5 nm)/Co(0.6 nm)/Fe₅₀Mn₅₀(X)/Ta(5 nm) antidots are investigated by extraordinary Hall effect measurements at 5 K, where X varies in the (0–5.5) nm range. The substrate consists in a hexagonal array of holes, described by the pair of (p, d) values, respectively, the period as the distance from center to center of two consecutive holes and the hole diameter. The dimensions of antidots are ($p \approx 100$ and $d \approx 40$ nm) for $X = (2-5.5)$ nm, ($p \approx 150$ and $d \approx 60$ nm) for $X = 3.5$ nm, and ($p \approx 100$ and $d \approx 60$ nm) for $X = 0$. A continuous stack using Si/SiO₂(100 nm) is used for comparison. H_C and $|H_{EXC}|$ gradually increase when X is enhanced for both substrates, with nevertheless a weak decrease at high X for the continuous system. Perpendicular magnetic anisotropy is only observed for both unbiased samples, the $X = 2$ nm continuous sample, and both $X = 5$ nm samples that have undergone field cooling treatment from 500 to 5 K under -2 T. Usually, $H_C(\text{AAO}) > H_C(\text{CML})$, $|H_{EXC}(\text{AAO})| > |H_{EXC}(\text{CML})|$, and $|H_A(\text{AAO})| < |H_A(\text{CML})|$ (H_A designating the anisotropy field). However, for certain conditions, as, for instance, for FC-procedures starting from high temperatures and/or strong magnetic field, other situations might be observed. A discussion pertaining to the amplitudes of H_C , $|H_{EXC}|$ and the anisotropy field ($|H_A|$) of continuous and discontinuous samples is given for our experimental results as well as for published data in the literature, in the light of structural characteristics (wedge-to-wedge distance, porosity, or coverage ratio). Such biased perpendicular antidots might be particularly used in specific nanomaterials devoted to spintronics.

Published under an exclusive license by AIP Publishing. <https://doi.org/10.1063/5.0173469>

I. INTRODUCTION

By reducing the size of magnetic materials, interesting physical properties that are potentially useful for applications might be induced.¹ For instance, a marked enhancement of the coercivity H_C ² and the exchange bias H_{EXC} ,³ when ferromagnets and antiferromagnets are combined leading to an antiferromagnetic coupling, is obtained in the magnetic hysteresis. In these two previous references, a lithographic process is used resulting in a discontinuous magnetic layer containing nonmagnetic holes called antidots. The two relevant physical parameters are the pore size, namely, d , and the period or the spacing between two consecutive holes from center to center,

namely, p . For instance, d and p are sensibly higher than 100 nm in the two previously mentioned studies.^{2,3} As a new potential interest of antidots, magnetic studies have established the generation of magnetic skyrmions in an antidot multilayered [Pt/Co/Ta]₁₂ with perpendicular magnetic anisotropy and Dzyaloshinskii–Moriya interactions (DMIs),⁴ or a continuous soft ferromagnetic film coupled to a hard magnetic antidot matrix with exchange and dipolar interactions, without any DMI, from micromagnetic simulations.^{5–7}

In the aim to reduce these lengths, Masuda and Fukuda⁸ have pioneered the fabrication of d lower than 100 nm by using chemical methods based on a two-step anodization method. For biased

55 planar antidots^{9–14} using such nano-templates, the authors claim
56 that the magnetic properties of antidots elaborated by this chemical
57 process might be understood by considering the pinning effects
58 around the nanoholes. As a result, the hysteresis loop is systemati-
59 cally more slanted for an applied magnetic field in the planar easy
60 direction; H_C ^{9–11,13,14} and H_A ¹⁰ are, respectively, increased and
61 lowered for the antidot, by comparison with the continuous film.
62 Concerning H_{EXC} , there seems to be contradictory results. The bias
63 field might be weaker,^{9,12} or higher,^{10,11,13,14} or have a complex
64 dependence on the ferromagnetic layer,¹² for the network structure
65 comparatively with the unholed sample.

66 In the case of unbiased perpendicular antidots,^{15–20} the
67 reduction of the perpendicular magnetic anisotropy is also
68 obtained, when the holed sample is used. As for planar systems, an
69 increase in H_C is also reported, for [Co(0.5 nm)/Pt(2 nm)]₅,¹⁵
70 CoCrPt[(5–20 nm)],¹⁶ TbCo(30 nm),¹⁷ DyFe^{18,19} (≈ 25 –30 nm),
71 and [Co(0.5 nm)/Pd(1 nm)]₅²⁰ antidots. Finally, perpendicular
72 biased antidots are seldom studied in the literature, as, for instance,
73 in some isolated Refs. 21–24, where Co(0.5 nm)/Pd(0.5 nm) multi-
74 layers exchange-coupled with an IrMn layer^{21–23} and a Co(0.5 nm)/
75 Pt(1 nm) multilayer coupled to IrMn²⁴ are studied. An enhance-
76 ment of the bias field is reported in both references, whereas the
77 coercivity is either diminished²⁴ or enhanced^{21–23} by using the
78 antidot structure.

79 Unfortunately, in these mentioned references, the value of H_A
80 (or K_{eff} the effective anisotropy constant) is not systematically eval-
81 uated based on magnetic measurements (for instance, any values
82 are indicated in Refs. 9, 11, 12, 13, 15, 16, 21, 22, 23, and 24).
83 Moreover, contradictory results appear for H_C and H_{EXC} when the
84 patterned and the continuous structures are compared. In the
85 present study, we address these contradictions, thanks to a system-
86 atic approach, and highlight the role of the magnetic atomic frac-
87 tions in the valley and on the top of the nanopores, on the
88 magnetic characteristics (coercive, exchange fields, effective anisot-
89 ropoly constant) for a series of exchange-coupled Ta/Pt/Co/FeMn/Ta
90 antidots by intensive extraordinary Hall effect (EHE) measure-
91 ments at 5 K. And we also give possible explanations to the contra-
92 dictory results published in the literature in the light of our own
93 findings by discussing the influence of structural characteristics
94 (such as wedge-to-wedge distance or porosity, for instance).

95 II. EXPERIMENTAL DETAILS AND STRUCTURAL 96 CHARACTERIZATIONS OF ANTIDOTS

97 The fabrication method of antidot arrays, detailed in Ref. 25,
98 uses a particular procedure as largely employed in the literature. In
99 order to prepare antidot arrays, an anodic alumina membrane was
100 prepared by the so-called two-step anodization process.⁸ After
101 mechanically polishing a mirror-like aspect and electropolishing at
102 30 V for 2 min in a perchloric acid/methanol mixture (1/4 in
103 volume) at 0 °C, high-purity (99.999%) aluminum foils were anod-
104 ized in a 0.5M oxalic acid with a constant potential of 40 V and
105 temperature around 16 °C. The first and second anodization were
106 performed during 17 and 7 h, respectively, which led to templates
107 with a thickness of 60 μm , and hole diameter and interpore dis-
108 tance around 40 and 100 nm, respectively. The obtained free-
109 standing nanoporous membranes are subject to a pore opening/

widening treatment in a phosphoric acid solution at 35 °C was
110 applied during an etching time (namely, $t_{etching}$) that was varied
111 between typically 30 and 90 min. This procedure allows the
112 removal of the barrier layer closing the bottom of the pores and
113 permitted us to obtain a pore diameter close to the native one of
114 $d = 40$ nm for $t_{etching} = 30$ min. For a longer $t_{etching}$ of 60 min, a
115 higher d is achieved (≈ 60 nm). As a consequence, two holed sub-
116 strates of the studied series in this paper are chosen ($d \approx 40$ and
117 $d \approx 60$ nm where $p \approx 100$ nm). Finally, a third type of holed sub-
118 strate is investigated where the period is higher, typically
119 $p = 150$ nm and for comparable d . This latter substrate was
120 obtained in the same oxalic acid solution but with a two-step anod-
121 izing process of 2 h, but at a higher voltage of $V = 60$ V. At this
122 voltage, the alumina growth rate is increased by a factor almost 3
123 compared to what is obtained at 40 V (due to the linearity of p
124 with V as $p = 2.5 \times V$ as detailed, for example, in Ref. 26). At the
125 same time, the hole diameter is also increased from 40 to 60 nm
126 [the relation between d and V as $d = 1.3 \times V^{26}$ is also checked].
127 With these conditions, a less well self-organized array with dis-
128 torted pore openings is obtained. For instance, a poor regularity of
129 a pore arrangement is seen after a second anodization step in the
130 0.3M oxalic acid solution at 2 °C under anodizing voltages of 60 V
131 in Ref. 27. Three kinds of substrates are used in the following of the
132 study: ($d \approx 40$ nm, $p \approx 100$ nm), ($d \approx 60$ nm, $p \approx 100$ nm), and
133 ($d \approx 60$ nm, $p \approx 150$ nm).
134

135 Then, each holed substrate is placed with a continuous sub-
136 strate Si/SiO₂(100 nm) on the sample holder during the sputtering
137 process, which features a base pressure of about 6.0×10^{-8} mbar,
138 an Ar pressure of 3.0×10^{-3} mbar during deposition, deposition
139 temperature ≈ 20 °C, and 0.05, 0.07, 0.09, and 0.1 nm/s as deposi-
140 tion rates for Co, FeMn, Pt, and Ta, respectively. As published in
141 Ref. 15, a Co thickness of 0.5 nm induces a perpendicular magnetic
142 anisotropy in [Co(0.5)/Pt(2)]₅ multilayers [the thicknesses in
143 parentheses being expressed in nm]. Moreover, an optimization of
144 the bias field and the coercivity at RT by varying the Co thickness
145 (X) has been observed in Ta(5)/Pt(2)/Co(X)/FeMn(4)/[Ta(3) or Pt
146 (3)] multilayers for $X \approx 0.4$ nm.²⁸ With this in mind, we focus on
147 systems with a close enough Co thickness value of 0.6 nm in that
148 present study. We have employed Ta as seed layer due to its (111)
149 texture, inducing a similar texture for the (Pt, Co, FeMn) subse-
150 quent layers, which favors perpendicular exchange bias.²⁹ Unbiased
151 Ta(5)/Pt(5)/Co(0.6)/Ta(5) and biased Ta(5)/Pt(5)/Co(0.6)/
152 Fe₅₀Mn₅₀(X)/Ta(5) were sputtered on continuous and holed sub-
153 strates, where $X = (0-2-3.5-5.5)$ nm. Here, the error in the deter-
154 mination of the thickness is estimated to be $\pm 10\%$. The nominal
155 dimensions of antidots are ($p \approx 100$ and $d \approx 40$ nm) for $X = (2.0-$
156 $5.5)$ nm, ($p \approx 150$ and $d \approx 60$ nm) for $X = 3.5$ nm, and ($p \approx 100$
157 and $d \approx 60$ nm) for $X = 0$ nm. In order to ensure better visibility
158 of results, the magnetic data for antidots and continuous multi-
159 layers are plotted in black lines and red lines, respectively.

160 Typical SEM view of samples are given in Figs. 1(a)–1(d). The
161 presence of nanopore arrays arranged in a hexagonal way is con-
162 firmed, and no significant reduction in the pore diameter is
163 observed after completion of the film. Some dislocations are visible
164 in the network as appeared in these SEM figures, as expected by
165 using such nanosubstrates. In addition, circular shapes and ellipti-
166 cal ones are detected in Figs. 1(a), (b), and (d) and 1(c), 166

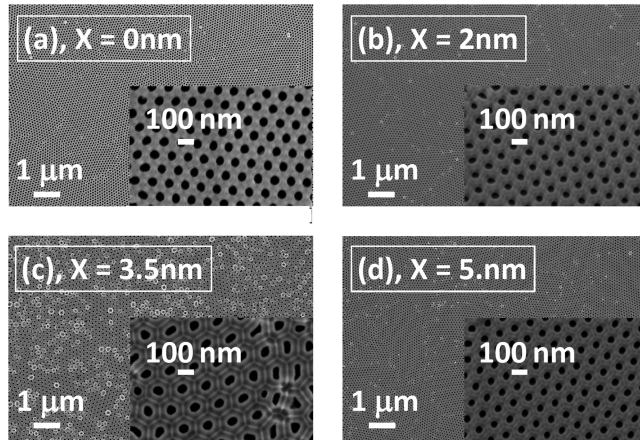


FIG. 1. (a) SEM views of Ta(5 nm)/Pt(5 nm)/Co(0.6 nm)/Fe₅₀Mn₅₀(X)/Ta(5 nm) antidots (thickness in nm) for different FeMn thicknesses X ranging from 0 to 5.5 nm. The mean period p as the distance from center to center of two consecutive holes and the mean diameter d are the dimensions of antidots are ($p \approx 100$ and $d \approx 40$ nm) for $X = (2-5.5)$ nm, ($p \approx 150$ and $d \approx 60$ nm) for $X = 3.5$ nm, and ($p \approx 100$ and $d \approx 60$ nm) for $X = 0$ nm. Note the elliptical shape of holes in (c) and circular ones in (a, b, and d).

167 respectively. This particular shape of ellipses has been reported in
168 Ref. 30 where authors have used the porous alumina as masks for
169 the deposition of ordered ferromagnetic nanodot arrays. For our
170 sample where $p \approx 150$ and $d \approx 60$ nm, the distortion of the hexagonal
171 arrangement of spherical pores is explained by the use of high
172 anodizing voltage (60 V), as in the published studies.^{27,31}

173 Coming back to the pore networks, the size distribution of
174 both p and d is given in Fig. 2 for these antidots by taking into
175 account the holes appearing in insets of Fig. 1. To do this, a conversion
176 of grayscale SEM images to binary black-and-white images
177 is performed. The pixels with grayscale values exceeding a threshold
178 are set to black, all others are set to white. The threshold values
179 are manually chosen so that the black areas in the black-and-white
180 images reproduce the pores in the original grayscale images. NIH
181 IMAGEJ software package is used to measure p and d , as well as
182 their standard deviations. The values of mean diameter d_{mean} ,
183 mean period p_{mean} , mean spacer s_{mean} between two consecutive
184 holes, and density of holes δ are gathered in Table I. Periodicity of
185 $p \approx 100$ and $p \approx 150$ nm is calculated starting from the distributions,
186 as well as holes density reaching $1.1 \cdot 10^{10}$ and $0.5 \cdot 10^{10}$ holes/
187 cm², in Figs. 1(a), (b), and (d) and 1(c), respectively. The size distribution
188 of pores is peaked around $d \approx 40$ and $d \approx 55$ nm, in
189 Figs. 1(b)–1(d) and Figs. 1(a)–1(c), respectively. Since the shape of
190 hole is elliptical in Fig. 1(c), a size distribution of ellipses is
191 assumed and the average length ratio (defined as minor axis/major
192 axis = b_{mean}/a_{mean}) reaches 0.67. As expected, we retrieve that the
193 area of the mean circle $\{(\pi/4) \times d_{mean}^2 = 2.445 \cdot 10^3 \text{ nm}^2\}$ is close to
194 the one of a mean ellipse $\{\pi \times (a_{mean} \times b_{mean})/4 = 2.435 \cdot 10^3 \text{ nm}^2\}$.
195 The size distribution is broader for the 3.5 nm multilayer.
196 Moreover, this 3.5 nm multilayer contains spacing between two
197 consecutive nanoholes more important than ones of the other

multilayers, indicating that more ferromagnetic material is deposited
198 on the top of multilayers compared to the ones elaborated on
199 the vicinity of nanoholes. This finding is important for magnetic
200 results, as developed in the following of the paper. 201

The extraordinary (also called anomalous) Hall effects (EHEs)
202 are currently described by a phenomenological equation expressing a
203 resistance as a function of different terms as $EHE = R_o \times H$
204 $+ R_e \times M_Z$, where H designates the external magnetic field, M_Z the
205 perpendicular magnetization, R_o the ordinary or normal coefficient,
206 and R_e the extraordinary Hall one. In case of materials with marked
207 spin-orbit scattering such as the case of our materials (Pt/Co), the
208 second term ($R_e \times M_Z$) dominates the first one ($R_o \times H$). As a consequence,
209 this kind of measurement is a direct signature of the
210 perpendicular magnetization as a function of applied magnetic field,
211 a magnetic loop being obtained. Experimental and
212 theoretical approaches are found in a review paper devoted to
213 EHE.³² For the practical measurements, a cross Hall is used with a
214 line of current (typically a current of $I = 10 \mu\text{A}$) perpendicular to a
215 line of voltage (leading to a measurement of variation of voltage
216 ΔV). EHE is simply defined by $EHE = \Delta V/I$ (typically around 0.1Ω).
217 In this study, we have normalized the EHE response as
218 $M_Z^{norm}(H_Z) = [2EHE(H_Z) - (EHE_{max} + EHE_{min})]/\Delta R_{EHE}$, where H_Z
219 is the perpendicular magnetic field, $\Delta R_{EHE} = EHE_{max} - EHE_{min}$,
220 EHE_{max} and EHE_{min} being the maximum and minimum of resistance,
221 respectively. M_Z^{norm} varies between -1 and $+1$ as for the case
222 of a classical normalized hysteresis loop. ΔR_{EHE} designates the total
223 amplitude of the Hall signal. In the following, $M_Z^{norm}(H_Z)$ is recorded
224 at 5 K and for H_Z up to 3 T after zero field cooling (ZFC), or after
225 Field Cooling (FC) H_{FC} -FC(T_{max}). Here, H_{FC} and T_{max} designate the
226 magnetic field applied during the field cooling procedure and the
227 maximum of temperature before cooling. The blocking temperature
228 T_b for Fe₅₀Mn₅₀, temperature at which $H_{EXC} = 0$, was about
229 (390–480) K for relatively high or moderate FeMn thicknesses ($> a$
230 few nm),³³ or lower for thinner FeMn ones (< 1 nm).^{34,35} Thus, we
231 have fixed T_{max} at 500 K, and 300 K is also employed for comparison.
232 These measurements allow us to derive H_C and H_{EXC} . Then, after
233 the out-of-plane measurement, without extracting the sample
234 from the EHE setup, a second measurement is immediately performed
235 with field H_X up to 3 T, and applied parallel to the sample
236 plane with a very small misorientation ($\approx 2^\circ$) in order to ensure a
237 coherent rotation of the Co moments. The normalized in-plane component
238 of the magnetization M_X^{norm} is $(1 - [M_Z^{norm}]^2)^{0.5}$. The anisotropy
239 field H_A is determined from the area between perpendicular and
240 planar EHE measurements, and the latter is defined as $2 \int_0^{3T} dH$
241 $[M_Z^{norm}(H_Z^{mean}) - M_X^{norm}(H_X)]$, where M_Z^{norm} and M_X^{norm} are previously
242 recorded, H_Z^{mean} being the mean magnetic field defined by taking
243 into account the descending and ascending branches of the hysteresis
244 loop. Here, the maximum magnetic field 3 T is efficient for saturating
245 magnetic hysteresis. Concerning the effective anisotropy constant
246 K_{eff} , its value is calculated as $H_A \times (M_S/2)$ where M_S designates the
247 saturation magnetization of the sample measured at 5 K by SQUID. 248

III. INVESTIGATIONS OF MAGNETIC LOOPS AT 5 K 249

A. Unbiased stacks 250

After a ZFC procedure from RT to 5 K, M_Z vs H_Z (left part) 251
and M_X vs H_X (right part) at $T = 5$ K of 2 Ta/Pt/Co/Ta unbiased 252

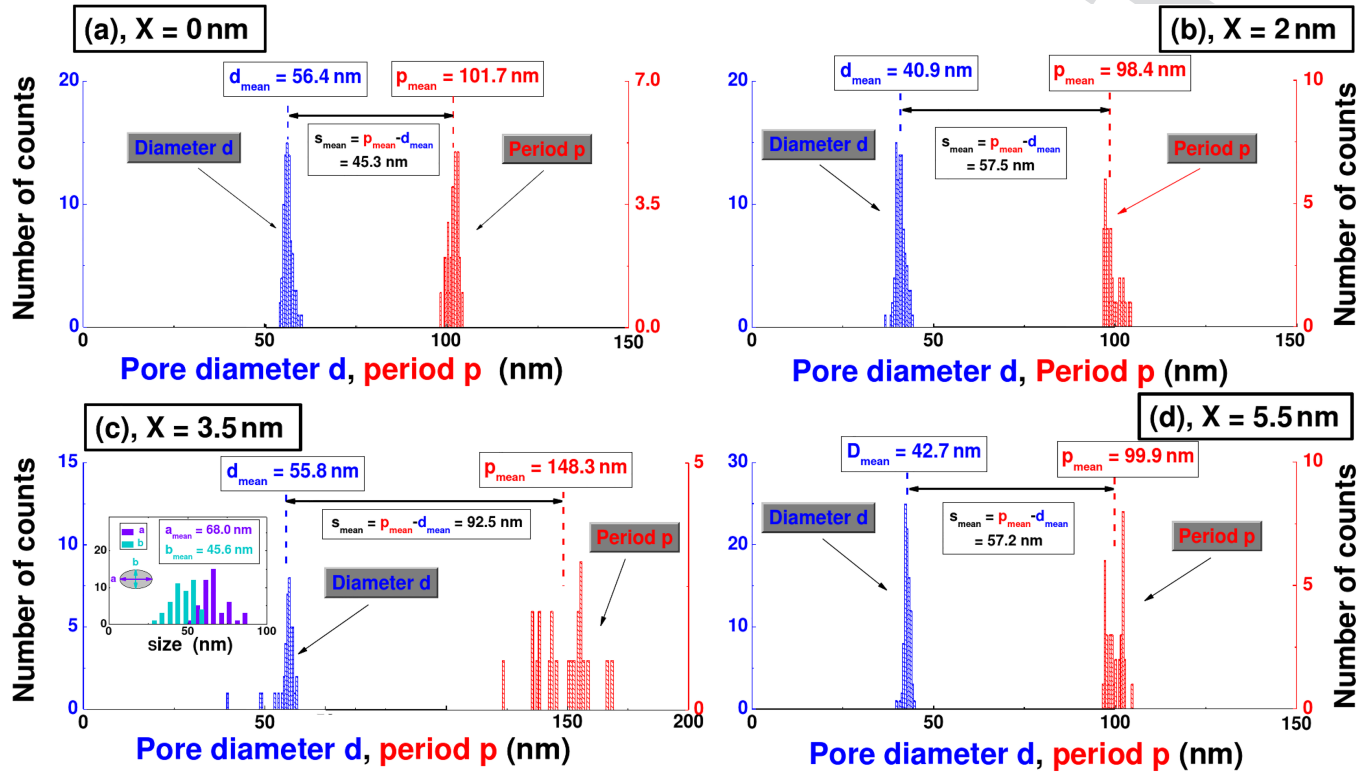


FIG. 2. (a) Distributions of periods p (distance from center to center of two consecutive holes), and hole diameter d deduced from Fig. 1 for Ta(5)/Pt(5)/Co(0.6)/Fe₅₀Mn₅₀(X)/Ta(5) antidots (thickness in nm) with FeMn thicknesses $X = (0-2-3.5-5.5)$ nm. In inset of (c) is plotted the distribution size of the minor and major axes of elliptical holes.

253 samples (antidot in black lines and continuous multilayer in red
254 lines) are displayed in Figs. 3(a) and 3(b), respectively. Here, the
255 dimension of the antidot is ($p \approx 100$ and $d \approx 60$ nm). A 3 kOe is
256 needed for saturating the magnetization in both directions of mag-
257 netic field. A clear square hysteresis for perpendicular magnetic
258 fields, as well as a hard axis for the planar H , are obtained for both
259 samples. In Fig. 3(a), the remanence M_R^+ reaches a high value
260 ($\approx 97\%$) for both data, and the saturation field (namely, H_{sat}^{\perp}),
261 defined as the field necessary for reaching 98.5% of the saturation
262 magnetization, is $H_{\text{sat}}^{\perp} = (2.346 - 2.780)$ kOe for the continuous

TABLE I. Structural characteristics of Ta(5)/Pt(5)/Co(0.6)/FeMn(X)/Ta(5) (thickness in nm) antidots where $X = (0-2-3.5-5.5)$ nm: nominal FeMn thickness X , mean diameter d_{mean} , mean period p_{mean} , mean distance s_{mean} between two consecutive holes, and density of holes δ . The standard deviations are indicated in parentheses.

X (nm)	d_{mean} (nm)	p_{mean} (nm)	s_{mean} (nm)	δ (10^{10} holes/cm 2)
0	56.4(1.1)	101.7(1.3)	45.3(1.5)	1.044(0.027)
2	40.9(1.3)	98.4(3.1)	57.5(3.6)	1.086(0.135)
3.5	55.8(3.3)	148.3(10.9)	92.5(12.3)	0.490(0.065)
5.5	42.7(0.8)	99.9(2.5)	57.2(2.5)	1.097(0.060)

263 multilayer and antidot, respectively. The different characteristics of
264 magnetic hysteresis (remanence, coercivity, bias field, maximum of
265 susceptibility, saturation field, anisotropy field, effective anisotropy
266 constant) are gathered in Table II. From the planar measurement
267 in Fig. 3(b), it appears that the saturation field (H_{sat}^{\perp} , see Table II) is
268 reached for lower magnetic field compared to the discontinuous
269 multilayer. In addition, by defining the susceptibility χ as $\frac{dM}{dH}$ (the
270 derivative of M following H), the maximum susceptibility for
271 $H \approx H_C$, namely, χ_{max} , is calculated for the stacks. We find
272 $\chi_{\text{max}}^{\parallel} \approx 1.2 \cdot 10^{-4} \text{Oe}^{-1}$ and $\chi_{\text{max}}^{\perp} \approx 3 \cdot 10^{-2} \text{Oe}^{-1}$ for these samples.
273 These features indicate that $H_A(\text{AAO}) < H_A(\text{CML})$. Concerning the
274 anisotropy field, we first apply the approximate method of linear
275 extrapolation of the EHE signal (in the high field regime) as was
276 done, e.g., in Ref. 36, and we find $H_A(\text{AAO}) \approx 1.714$ kOe and H_A
277 (CML) ≈ 2.005 kOe [see Fig. 3(a)]. More precisely, from the
278 formula using the integration of EHE data [and by using
279 the averaged signal as plotted in dotted lines in Fig. 3(a)], H_A
280 (AAO) = 1.485 Oe and $H_A(\text{C}) = 2.165$ kOe are derived as indicated
281 in Table I. The effective anisotropy constants (K_{eff}) are calculated
282 from H_A and the saturation magnetization measured at 5 K by
283 SQUID (1250 emu/cm^3) and are listed in Table I. This method of
284 integration is more accurate than the one using the slope of the
285 magnetization $M(H)$ for a hard magnetic field as shown in

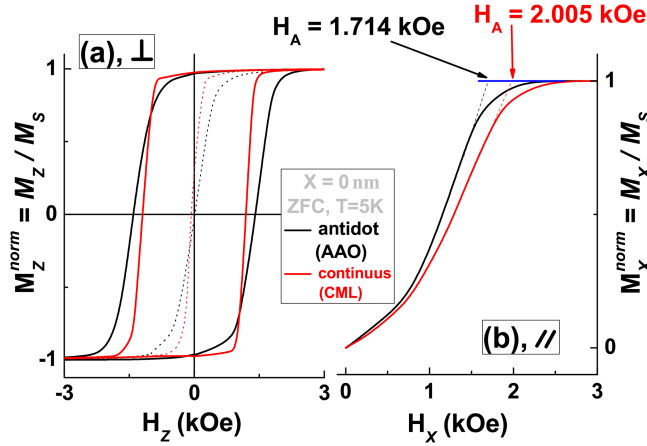


FIG. 3. Normalized extraordinary Hall effects $M_Z(H_Z)$ (a) and $M_X(H_X)$ (b) at 5 K after ZFC from RT to 5 K for the unbiased continuous multilayer (red lines) and the unbiased antidot (black lines). The stacking is Ta(5)/Pt(5)/Co(0.6)/Ta(5) (thickness in nm), and the dimension of the antidot is ($\rho \approx 100$ and $d \approx 55$ nm). The maximum magnetic field is 3 T and only 0.3 T is the maximum field of the graph for clarity of presentation. The dotted lines in (a) are the mean responses of data (decreasing and increasing branches), and the dashed linear extrapolation in (b) leads to a rough estimation of the anisotropy field (lower for the antidot structure).

286 Fig. 3(b). The reasons are that M is rarely linear in the complete
 287 range of *hard* before saturation, and $M(\text{easy } H)$ is not systemati-
 288 cally a perfect square loop, as the case for our samples. Other
 289 methods exist, such as the generalized Sucksmith–Thompson
 290 method,³⁷ which is less approximate than the method of the linear-
 291 ity of $M(\text{hard } H)$, but less accurate than the method of integration,
 292 could be employed. Concerning the coercive field H_C^\perp , its value is
 293 enhanced by using the antidot (1.418 kOe) compared to the contin-
 294 uous multilayer (1.194 kOe) as seen in Table II. As a result, the
 295 coercivity for H_{easy} (H aligned with the easy axis, namely, perpen-
 296 dicular to the layers) and the anisotropy field are, respectively,
 297 enhanced and reduced at 5 K when the antidot is used, as found in
 298 the literature^{15–17} for perpendicular systems. The probable reasons
 299 of the reduction of H_A (or the effective constant) and the enhance-
 300 ment of H_C^\perp are (i) the in-curved magnetic moments around
 301 nanopores,^{12,13,15,16,21–24} orientated almost in the plane of layers
 302 and perpendicularly to the out-of-plane applied magnetic field,
 303 provoking a reduction of the magnetic anisotropy; (ii) the pinning
 304 effects^{11–13,15,17} induced by the nanoholes leading to an increase in
 305 the coercive field. As expected, the magnetic data do not change
 306 when a FC procedure is applied for unbiased samples, and no bias
 307 fields H_{EXC}^\perp are recorded since no antiferromagnetic layer is grown
 308 on the sample (curves not shown).

309 B. Biased stacks with $T_{\text{max}} = 300$ K

310 After a ZFC procedure from RT to 5 K, M_Z vs H_Z (top part)
 311 and EHE_X vs H_X (bottom part) at $T = 5$ K for Ta/Pt/Co/FeMn(X)/
 312 Ta biased samples are displayed in Fig. 4, where $X = 2.0$ nm for
 313 [(a)–(d)], $X = 3.5$ nm for [(b)–(e)], and $X = 5.5$ nm for [(c)–(f)].

TABLE II. Magnetic characteristics extracted from EHE data for perpendicular (\perp) and planar (\parallel) magnetic fields for biased continuous multilayers and biased antidots deduced from Figs. 3 and 4. The stacking is Ta(5)/Pt(5)/Co(0.6)/FeMn(X)/Ta(5) where $X = (0-2-3.5-5.5)$ nm, the antidots being fabricated with dimensions of ($\rho = 100$ and $d = 55$ nm) for $X = (2-5.5)$ nm, and ($\rho = 150$ and $d = 55$ nm) for $X = 3.5$ nm. The magnetic and thermal procedure of measurements is either ZFC (zero field cooling from RT to 5 K) or FC (field cooling from RT or 500–5 K under $(+1, +2, -2)$ T), M_R ($\pm 3\%$), H_C (Oe, $\pm 7\%$), H_{EXC}^\perp (Oe, $\pm 5\%$), H_A (Oe, $\pm 4\%$), and K_{eff} (erg/cm^2 , $\pm 10\%$) designate the remanence, coercivity, exchange bias, maximum of susceptibility, saturation field, anisotropy field, and effective anisotropy constant, respectively. Here, “No” means the absence of measurements.

Samples	M_R^\perp (%)	H_C^\perp (10^3)	H_{EXC}^\perp	χ_{max}^\perp	$\chi_{\text{max}}^\parallel$	$\chi_{\text{max}}^\perp / \chi_{\text{max}}^\parallel$	H_{sat}^\perp (10^3)	H_{sat}^\parallel (10^3)	H_A (10^3)	K_{eff} (10^6)
$X = 0$ nm, continuous, ZFC	97.4	1.194	1.7	3.6×10^{-2}	3.6×10^{-2}	No	2.346	2.300	2.165	1.353
$X = 0$ nm, antidot, ZFC	96.5	1.418	2.5	2.2×10^{-2}	2.2×10^{-2}	No	2.780	1.993	1.485	0.928
$X = 2$ nm, continuous, ZFC	75.4	2.820	-24.2	3.4×10^{-4}	3.4×10^{-4}	No	10.532	7.516	0.410	0.256
$X = 2$ nm, antidot, ZFC	63.6	2.517	-127.0	3.5×10^{-4}	3.5×10^{-4}	No	12.030	3.352	-2.139	-1.337
$X = 3.5$ nm, continuous, ZFC	41.7	3.226	-57.6	1.4×10^{-4}	1.4×10^{-4}	No	17.889	12.010	-5.167	-3.230
$X = 3.5$ nm, antidot, ZFC	61.6	2.625	-196.7	3.4×10^{-4}	3.4×10^{-4}	No	13.519	5.520	-2.127	-1.329
$X = 3.5$ nm, continuous, IT-FC(RT)	59.3	5.034	-3239.3	1.9×10^{-4}	1.9×10^{-4}	No	18.324	No	No	No
$X = 3.5$ nm, antidot, IT-FC(RT)	61.5	2.614	-299.3	3.4×10^{-4}	3.4×10^{-4}	No	14.084	No	No	No
$X = 5.5$ nm, continuous, ZFC	39.2	2.501	-38.7	1.9×10^{-4}	1.9×10^{-4}	No	19.426	9.894	-5.136	-3.210
$X = 5.5$ nm, antidot, ZFC	48.6	3.338	-495.7	2.0×10^{-4}	2.0×10^{-4}	No	24.381	10.941	-4.830	-3.019
$X = 5.5$ nm, continuous, IT-FC(RT)	55.4	3.967	-2879.3	2.4×10^{-4}	2.4×10^{-4}	No	16.540	No	No	No
$X = 5.5$ nm, antidot, 2T-FC(500 K)	50.8	2.966	-1165.6	2.3×10^{-4}	2.3×10^{-4}	No	21.196	No	No	No
$X = 5.5$ nm, continuous, -2T-FC(500 K)	62.0	4.400	+2156.9	2.4×10^{-4}	2.4×10^{-4}	No	23.180	15.008	4.179	2.61
$X = 5.5$ nm, antidot, -2T-FC(500 K)	52.3	3.335	+778.6	1.9×10^{-4}	1.9×10^{-4}	No	20.801	18.871	1.930	1.206

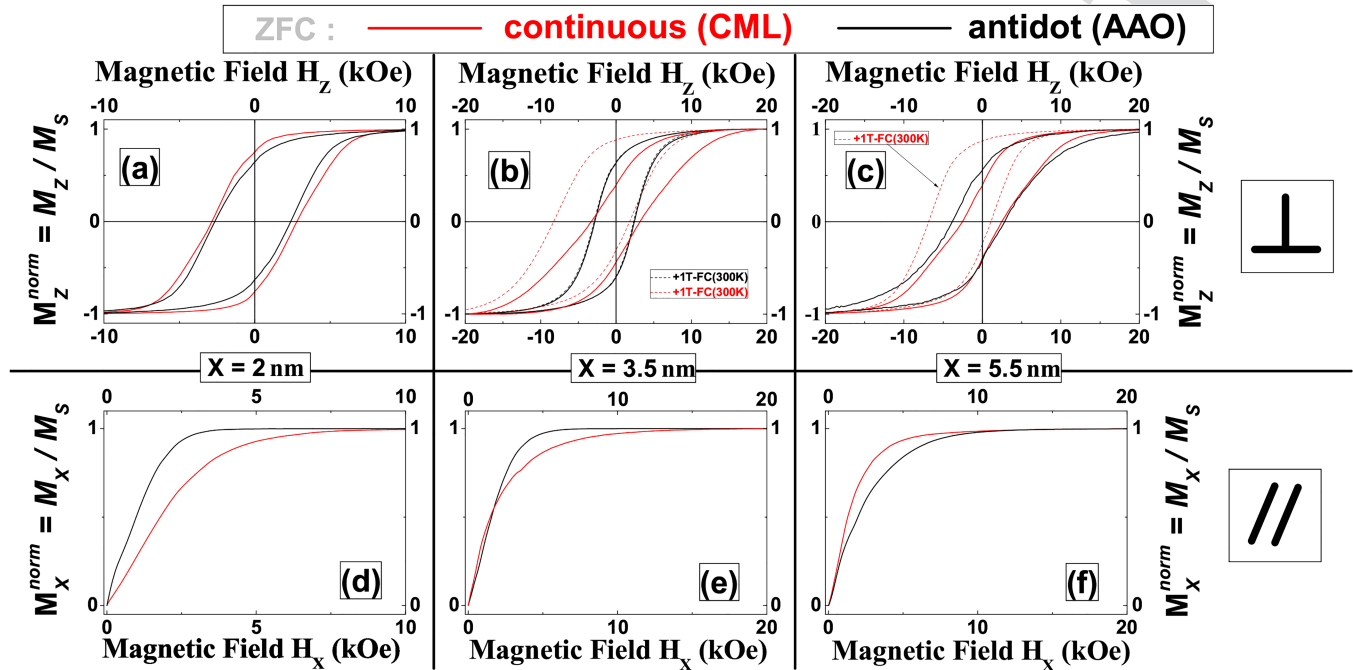


FIG. 4. Normalized extraordinary Hall effects $M_Z(H_Z)$ [(a)–(c), top panel] and $M_X(H_X)$ [(d)–(f), bottom panel] at 5 K for biased continuous multilayers (red lines) and biased antidots (black lines), after ZFC procedures. The stacking is Ta(5)/Pt(5)/Co(0.6)/FeMn(X)/Ta(5) (thickness in nm) where $X = 2$ nm for [(a)–(d)], $X = 3.5$ nm for [(b)–(e)], and $X = 5.5$ nm for [(c)–(f)]. The maximum magnetic field is 3 T and the dimensions of antidots are ($p = 100$ and $d = 40$ nm) for $X = (2\text{--}5.5)$ nm and ($p = 150$ and $d = 55$ nm) for $X = 3.5$ nm. $H_{FC}\text{-FC}(T_{\max})$ data are added in (b) and (c) for comparison, where $H_{FC} = 1$ T and $T_{\max} = 300$ K designate the magnetic field applied during the Field Cooling procedure and the maximum of temperature before cooling.

314 The data for antidots and continuous multilayers are plotted in
315 black lines and red lines, respectively.

316 We first concentrate on the lowest FeMn thickness
317 [$X = 2$ nm, Figs. 4(a)–4(d)]. The magnetic field necessary for saturating
318 the magnetic hysteresis is 1 T, meaning that a higher H is
319 necessary when a biased sample is measured [0.3 T was necessary
320 for the unbiased samples as plotted in Fig. 4(a)]. For this lowest
321 FeMn thickness, slanted $M(H)$ magnetic loops are recorded, the
322 susceptibility and the remanence reach $\chi_{\max}^{\perp} \approx 3.4 \cdot 10^{-4} \text{Oe}^{-1}$ and
323 $M_R^{\perp} \approx 70\%$, respectively, for both samples (as merged in Table II).
324 As a consequence, the remanence and the maximum susceptibility
325 are reduced when a FeMn layer is added to the sample, and weak
326 differences seem to appear for the two biased samples. Concerning
327 the saturation field for perpendicular magnetic data, H_{sat}^{\perp}
328 is increased for the antidot (12.030 kOe) compared to the continuous
329 structure (10.532 kOe). In the same way, for planar magnetic H
330 [see Fig. 4(d)], $M(H)$ saturates at larger applied fields for the
331 $X = 2$ nm continuous sample ($H_{\text{sat}}^{\parallel} = 7.516$ kOe), accompanied by
332 a weak slope of the hysteresis ($\chi_{\max}^{\parallel} = 4.0 \cdot 10^{-4} \text{Oe}^{-1}$), indicating
333 that, by combining the results from configurations of magnetic
334 fields, H_A seems to be higher for the continuous multilayer than
335 the antidot as expected. Surprisingly, from the integration method,
336 $H_A = -2.139$ kOe and $H_A = +0.410$ kOe for the antidot and the
337 continuous multilayer, respectively. This result means that a spin
338 reorientation transition driven by the substrate geometry takes

339 place for the $X = 2$ nm biased sample, from a planar magnetic
340 anisotropy for the antidot to a perpendicular one for the continu-
341 ous multilayer. Here, there are probably different contributions to
342 the magnetic switching mechanism for this sample. By comparing
343 magnetization curves calculated using an appropriate switching
344 model with measured ones, it will be possible to determine these
345 contributions (another study).

346 The reverse situation has been reported in the literature for
347 films deposited on nanoporous alumina membranes, as the form
348 $\text{Dy}_{13}\text{Fe}_{87}(30 \text{ nm})$ with $d = 45$ nm and $p = 105$ nm,^{18,19} where the
349 easy axis of the magnetization is laying along the planar direction for
350 the continuous stack whereas it is out-of-plane for the antidot array.
351 A similar result was also observed for samples by Gräfe *et al.* in Fe
352 (200 nm) antidot arrays ($d = 100$ and $p = 200$ nm) fabricated by
353 nanosphere lithography.³⁸ At our knowledge, it is the first time that
354 PMA is suppressed for an exchange-coupled continuous system
355 (with, in particular, a weak anisotropy field) by using an antidot as
356 substrate. The last striking characteristic of Fig. 4(a) is that
357 $H_C^{\perp} = (2.820/2.517)$ kOe and $H_{\text{EXC}}^{\perp} = (-24.2/-127.0)$ Oe for the
358 (CML/AAO) samples pair. Thus, the coercive field is lowered when
359 the antidot is used, similarly to Ref. 24 but in contrast to Refs. 21–23,
360 an increase in the bias field with antidots is confirmed.^{21–24}

361 Now, we come to discuss the EHE results for the higher FeMn
362 thicknesses. For $X = 3.5$ nm, the magnetic loop for the ZFC data
363 [see Fig. 4(b)] is more slanted for the continuous structure with a

364 reduction of the remanence (M_R^\perp , 61.6– 41.7%) and the susceptibility
365 (χ_{\max}^\perp , 3.4×10^{-4} to $1.4 \times 10^{-4} \text{Oe}^{-1}$) accompanied by an enhance-
366 ment of the saturation field (H_{sat}^\perp , 13.519–17.889 kOe), from the
367 discontinuous to the continuous system. Similarly, the planar sus-
368 ceptibility and the planar saturation field increase from the antidot to
369 the unholed substrate, respectively, $\chi_{\max}^{\parallel} = (3.1 \cdot 10^{-4}/4.4 \cdot 10^{-4}) \text{Oe}^{-1}$
370 and $H_{\text{sat}}^{\parallel} = (5.520/12.010) \text{kOe}$. At a first sight, this is an intrigu-
371 ing discrepancy between our results and some published in the litera-
372 ture where $M(H)$ are more slanted for antidots rather than
373 continuous substrates. In fact, as indicated by the values of rema-
374 nence and saturation field for both configuration of magnetic fields,
375 the easy axis of the magnetization seems to be in plane. Indeed, the
376 anisotropy fields are evaluated from the method of integration: H_A
377 (AAO) = -2.127kOe and $H_A(\text{CML}) = -5.167 \text{kOe}$. As a conse-
378 quence, for both $X = 3.5 \text{ nm}$ samples, the magnetic anisotropy is
379 planar due to the FeMn layer which forces the Co pinned spins to be
380 in the plane of layers. Nevertheless, for perpendicular magnetic fields
381 (H), the Co spins around holes are parallel to H and force in part
382 the magnetization to be out-of-plane. For the continuous sample,
383 majority planar Co spins exchange-coupled with antiferromagnetic
384 FeMn spins induce the easy axis of the magnetization to be more
385 planar. This is the reason why planar magnetic anisotropy is
386 observed for both samples and $|H_A(\text{AAO})| < |H_A(\text{CML})|$. Then, for
387 a hard axis of the magnetic field, the $M(H)$ magnetic loops are more
388 in-curved for the continuous structure. This feature has been
389 observed in the literature for perpendicular antidot arrays, as
390 $[\text{Co}(0.5 \text{ nm})/\text{Pt}(20 \text{ nm})]_5^{15}$ over a wide range of diameters from 7 to
391 46 nm, $\text{CoCrPt}(10 \text{ nm})^{16}$ and $\text{DyFe}(30 \text{ nm})^{18,19}$ where the $M(H)$
392 magnetic loop is more slanted for the continuous film when the
393 magnetic field is applied in the plane of layers (hard axis of the mag-
394 netization). Concerning the coercivity and exchange bias, its values
395 are, respectively, lowered and enhanced (in accordance with
396 Refs. 21–24) when the antidot is used as indicated in Table II, simi-
397 larly to the $X = 20 \text{ nm}$ sample. This result indicates that both
398 $X = 2 \text{ nm}$ and $X = 3.5 \text{ nm}$ stacks have similar behaviors for coerciv-
399 ity and bias field due to the fact that probably the antiferromagnetic
400 thickness is too weak to efficiently induce exchange coupling, at least
401 for ZFC measurements. At first glance, the behaviors of coercivity
402 and exchange fields with the antiferromagnetic thickness for our
403 samples are consistent with the results published in the literature.¹³
404 Nevertheless, by comparing both coercivity and bias fields for the
405 two types of substrates, the results are contrast to same Refs. 21– 23.
406 We will come back to the possible reasons for explaining these pecu-
407 liar results about H_C^\perp , H_{EXC}^\perp , as well as H_A in the discussion part
408 (Sec. IV).

409 The effect of a FC procedure on the $M(H)$ cycle for both
410 biased antidots and continuous multilayer is scarce in the literature,
411 such as in Refs. 22 and 23 for $[\text{Co}(0.5 \text{ nm})/\text{Pd}(1 \text{ nm})]_5/\text{IrMn}(6 \text{ nm})$
412 (with the appearance of a weak bias value, 270 Oe). For the
413 $X = 3.5 \text{ nm}$ samples (antidot and continuous), a +1T-FC proce-
414 dure has been performed from RT to 5 K as shown in dashed lines
415 in Fig. 4(b), since noticeable exchange bias effects have been mea-
416 sured for this multilayer. As the blocking temperatures for these
417 samples might be comparable with the room temperature^{34,35} due
418 to the weak thickness of FeMn, we can suspect eventual modifica-
419 tions of $M(H)$ loops between ZFC and FC data. Indeed, for the
420 continuous structure, the magnetic hysteresis is more squared with

an increase of M_R^\perp and χ_{\max}^\perp . The bias $|H_{\text{EXC}}^\perp|$ and coercive H_C^\perp
fields have clearly increased from 57.6 to 3239.3 Oe and from 3.226
to 5.034 kOe, respectively (see Table II), a saturation field seems to
be relatively constant ($H_{\text{sat}}^\perp \approx 18 \text{kOe}$). By contrast, very weak
changes between ZFC and FC data are observed for the antidot
sample with close values of coercivity, bias field, remanence, sus-
ceptibility, and saturation fields. As a result, during the FC proce-
dure from RT to 5 K under +1 T, magnetic spins of Co of the
unholed sample are partially tilted in the perpendicular axis along
the applied magnetic field. At the opposite, for the holed sample,
the spins are relatively pinned and/or the blocking temperature
could be higher than RT, and the applied magnetic has a weak
influence on the reorientation of the magnetization. As a conse-
quence, the bias is enhanced for the continuous structure compared
to the holed one, the pair of ratios $[H_C^\perp(\text{CML})/H_C^\perp(\text{AAO}), H_{\text{EXC}}^\perp(\text{CML})/H_{\text{EXC}}^\perp(\text{AAO})]$
enhancing from [1.2,0.3] for ZFC measure-
ments to [1.9,10.8] for FC ones.

Now, to reach saturation of the magnetic hysteresis of the
5.5 nm samples, it is necessary to apply 3 T as maximum fields.
Across the series of samples and focusing on the ZFC hysteresis
loops, we notice (i) a reduction of M_R^\perp and χ_{\max}^\perp and (ii) a rounding
of the $M(H)$ curves as X increases. The largest saturation fields
 H_{SAT}^\perp [$\approx (19.4 - 24.4) \text{kOe}$] are obtained for the $X = 5.5 \text{ nm}$
samples. In the same way, the bias field $-H_{\text{EXC}}^\perp$ and the coercive field
 H_C^\perp increase with X for the antidots. For the continuous structures,
 $(-H_{\text{EXC}}^\perp/H_C^\perp)$ seems to decrease between $X = 3.5$ and $X = 5.5 \text{ nm}$:
(57.6/3226) and (38.7/2501) Oe, respectively. These behaviors of
coercive and bias fields are coherent with published results in the lit-
erature at least for continuous structures,^{28,29,34} where FeMn is used
as an antiferromagnetic layer, and for holed systems¹³ (NiO as anti-
ferromagnetic layer). To our knowledge, no comparison between
both kind of substrates has been reported in the literature for biased
FM/FeMn systems with FM as a ferromagnetic layer and as a func-
tion of antiferromagnetic thicknesses. Moreover, by gathering per-
pendicular [Fig. 4(c)] and planar [Fig. 4(f)] ZFC EHE data, the
anisotropy field $-H_A$ is maximized, reaching 4.830 and 5.136 kOe
for the antidot and continuous 5.5 nm samples, respectively. This
result indicates planar magnetic anisotropy for the $X = 5.5 \text{ nm}$
samples. As for the $X = 3.5 \text{ nm}$ sample, by applying a +1 T-FC
procedure for the $X = 5.5 \text{ nm}$ continuous sample, the $M(H)$ mag-
netic loop [red dashed line in Fig. 4(c)] is more squared, with
higher χ_{\max}^\perp and M_R^\perp , coupled to lower H_{SAT}^\perp (see Table II). The
+1 T-FC procedure partially reinforces the out-of-plane magnetic
anisotropy for the continuous sample, accompanied by an enhance-
ment of couples of ratio $[H_C^\perp(\text{CML})/H_C^\perp(\text{AAO}), H_{\text{EXC}}^\perp(\text{CML})/H_{\text{EXC}}^\perp(\text{AAO})]$
from [0.7,0.08] for ZFC measurements to [1.3,2.5] for FC
ones. Since the FC procedure from 300 to 5 K has a strong influence
on only continuous structures with persisting in-plane magnetic
anisotropy for both substrates, the effect of a higher T_{max} (500 K) is
studied in the next part of the paper.

C. Biased stacks with $T_{\text{max}} = 500 \text{ K}$

Finally, a -2 T-FC procedure with $T_{\text{max}} = 500 \text{ K}$ has been
performed on both samples (see Fig. 5 in dotted lines). Once again,
some weak changes appear for the antidot by comparing with
 $-2 \text{ T-FC}(500 \text{ K})$ and ZFC data [see Fig. 4(c)], with, in particular, a

476 marked positive exchange bias (778.6 Oe) due to the negative value
477 of the applied magnetic field during cooling. For the 5.5 nm contin-
478 uous sample, an opening of the $M(H)$ loop appears with high rem-
479 nance (62.0%), strong coercivity (4.4 kOe), and bias field
480 (2.157 kOe). The remarkable result is the appearance of perpendic-
481 ular magnetic anisotropy for both samples, meaning that a spin
482 reorientation from planar to perpendicular takes place by choosing
483 the two types of substrate. For the 5.5 nm continuous sample, the
484 highest anisotropy field is extracted from magnetic data and
485 reaches 4.179 kOe. For the $X = 5.5$ nm holed structure, a +2 T-FC
486 procedure has been also tested with $T_{\max} = 500$ K above T_b [black
487 dashed line in Fig. 5(a)]. Weak changes are detected for this sample
488 between ZFC and FC data, except a marked enhancement of $-H_{EXC}^{\perp}$
489 from 495.7 to 1165.6 Oe, respectively. As a consequence, for a
490 maximum temperature higher than T_b , the field cooling from 500
491 to 5 K re-orientates the magnetization in a perpendicular configura-
492 tion due to the blocking temperature of the antidot lower than
493 500 K, with pronounced modifications of magnetic hysteresis (for
494 perpendicular magnetic H) on the continuous sample rather than
495 the antidot. The positive magnetic anisotropy is higher for the con-
496 tinuous stack by a factor of 2.

497 In addition, we believe that uncompensated spins at interfaces
498 between Co and FeMn are key parameters for the understanding of
499 underlying mechanism of antiferromagnetic domain formation.
500 Then, a x-ray magnetic circular dichroism study, as in Ref. 39 for
501 Ni/FeF₂, on the role of uncompensated spins to exchange bias for a
502 series of antidots when a unique structural parameter is varied (as,
503 for instance, d) could be useful in that sense.

504 D. Amplitude of the Hall resistance

505 The amplitudes of ΔR_{EHE} of antidots and continuous Ta/Pt/
506 Co/FeMn(X)/Ta as a function of X for ZFC data are displayed in

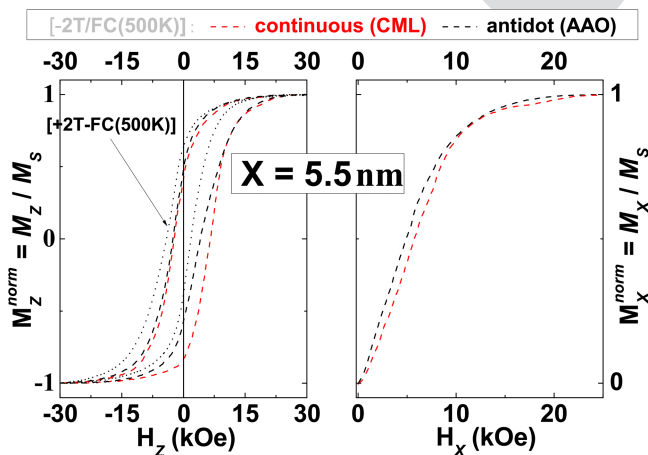


FIG. 5. Normalized extraordinary Hall effects $M_z(H_z)$ (a) and $M_x(H_x)$ (b) at 5 K after -2 T/FC from 500 to 5 K for the biased continuous multilayer (red lines) and the biased antidot (black lines). The stacking is Ta(5)/Pt(5)/Co(0.6)/FeMn(5.5)/Ta(5) (thickness in nm), and the dimension of the antidot is ($p = 100$ and $d = 40$ nm). The dotted lines in (a) are additional perpendicular data for +2 T/FC(500 K) for the antidot.

Fig. 6. The strongest value is recorded for the membrane, more X
and more ΔR_{EHE} is recorded for both substrates, except the
 $X = 3.5$ nm antidot. An increased Hall effect resistance in Pd/Co
antidots⁴⁰ and Co/Pd multilayered nanodomes⁴¹ has been attrib-
uted to the reduced number of available paths for the electric
current to flow through in the discontinuous sample. Such an
explanation of the increase in the total amplitude of the Hall signal
could be applied to our antidots. After +1 T/300 K procedure for
both 3.5 nm samples, ΔR_{EHE} is almost constant as appeared in
Fig. 6, revealing that the saturation magnetization is almost the
same after ZFC and FC procedures where $T_{\max} = 300$ K, since
 ΔR_{EHE} is in part proportional to the M_z component of the magneti-
zation. For the 5.5 nm samples, EHE_{\max} is lowered and increased
after FC procedures for the antidot and continuous structure.
respectively. Here, for the highest FeMn thickness (5.5 nm) and
continuous substrate, more out-of-plane magnetic domains due to
the FC procedure participate to the increase of the Hall signal.
More T_{\max} and/or H_{FC} are, more the amplitude of ΔR_{EHE} is
recorded. And for the membrane, even for high T_{\max} , ΔR_{EHE} is
weakly lowered. The magnetic field (+2 or -2 T) during the
FC-procedure do not reorientate the magnetic spins in the direc-
tion perpendicularly to the layers due to the pinning centers
around the edges of antidots, which force it in the circular direction
of the membrane.

531 IV. DISCUSSION

532 For a ZFC procedure, a sharp transition in the perpendicular
533 magnetic loop $M(H)$ at 5 K have been only observed for the

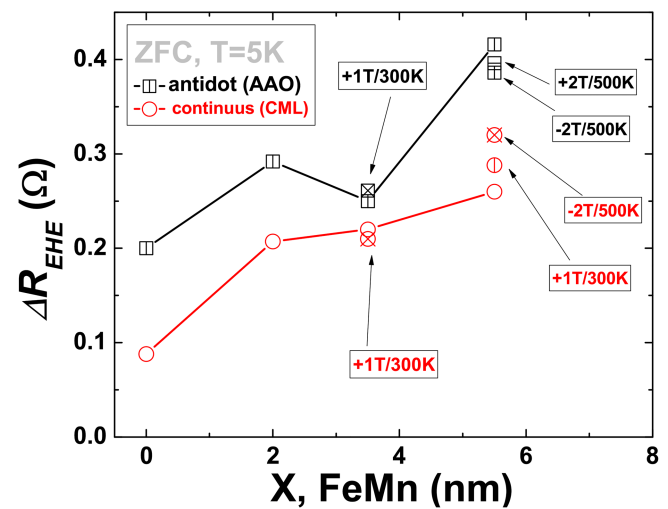


FIG. 6. ΔR_{EHE} ($=EHE_{\max} - EHE_{\min}$) vs FeMn thickness X at 5 K of Ta(5)/Pt(5)/Co(0.6)/FeMn(X)/Ta(5) antidots (AAO) and continuous multilayers (CMLs) for X in the (0 – 2 – 3.5 – 5.5) nm range. The dimensions of antidots are ($p = 100$ and $d = 55$ nm) for $X = 0$ nm, ($p = 100$ and $d = 40$ nm) for $X = (2 - 5.5)$ nm, and ($p = 150$ and $d = 55$ nm) for $X = 3.5$ nm. The data (empty symbols and cross symbols) are obtained after ZFC and FC procedures, respectively.

534 unbiased samples (continuous and antidot) and for the
535 $X = 2$ nm-continuous sample. This result suggests a switching by
536 domain wall motion only for these stacks where the easy axis is
537 perpendicular to the plane of layers. For the other biased samples,
538 more rounded shapes of $M(H)$ are detected for perpendicular mag-
539 netic fields due to the magnetization rotation process. Now, the
540 axis perpendicular to the layers planes becomes the hard axis for
541 the magnetization for both substrates. A simple Pt/Co/FeMn
542 system with perpendicular magnetic anisotropy is difficult to
543 obtain, as for the isolated Ref. 28 for Pt(2/Co(0.6)/FeMn
544 ($X > 4$ nm). By using a multilayer with a period $N > 1$ in a
545 (Pt/Co) $_N$ /FeMn, an easy perpendicular axis is induced, as, for
546 instance, in Ref. 42 for [Co(0.6)/Pt(2)] $_{N=5}$ /FeMn ($X > 4$ nm). For
547 the series of multilayers where $X = (0-3.5-5.5)$ nm, $|H_A(\text{anti-}$
548 $\text{dots})| < |H_A(\text{CML})|$ is obtained, whereas for $X = 2$ nm, $|H_A(\text{anti-}$
549 $\text{dots})| > |H_A(\text{CML})|$. For this particular sample (2 nm), a spin
550 re-orientation of the magnetic anisotropy from planar (for the
551 antidot sample where $H_A < 0$) to perpendicular (for the continu-
552 ous one where $H_A > 0$) is observed. Concerning exchange bias, we
553 have $|H_{EXC}(\text{antidots})| > |H_{EXC}(\text{CML})|$ for the whole series of struc-
554 tures. About the coercivity, $H_C(\text{antidots}) > H_C(\text{C})$ for no FeMn and
555 large FeMn thickness (5.5 nm), whereas $H_C(\text{antidots}) < H_C(\text{ML})$
556 for intermediate FeMn thickness (2 and 3.5 nm).

557 The remarkable result is when a FC procedure is employed
558 from high temperature (500 K) to 5 K with $H_{FC} = -2$ T, a new
559 spin reorientation appears for both 5.5 nm samples with the occur-
560 rence of PMA. The anisotropy field is stronger for the continuous
561 multilayer, similarly to the ZFC data. Now, the coercivity is the
562 highest for the continuous structure (as for the ZFC data for $X = 2$
563 and 3.5 nm) for an applied magnetic aligned with the easy perpen-
564 dicular axis. The magnetic field during the FC procedure favors the
565 appearance of PMA, as well as exchange bias and coercivity fields
566 (only for the continuous multilayer). Nevertheless, for the antidot,
567 the coercivity is almost constant between ZFC and FC data, reach-
568 ing 3.338 and 3.335 kOe, respectively.

569 In fact, films deposited on top of antidots are known to have a
570 crescent shape profile.⁴³ For instance, as developed in a previous
571 study in Cu/Co/Co antidots,⁴⁴ a two-step reversal process in the
572 magnetic loop is explained by a three-dimensional profile of the Co
573 magnetization due to both magnetic moments between nanopores
574 aligned within the film plane and magnetic moments along the
575 walls of the nanopores aligned perpendicular to the surface. As a
576 result, the surface morphology of the alumina membrane is a key
577 for understanding the magnetic properties. In Ref. 45, the authors
578 have succeeded in characterizing quantitatively both the reversible
579 and the irreversible magnetization processes in FePd antidots with
580 planar magnetic anisotropy. In these holed nanostructures, $d = 35$
581 and $p = 105$ nm, from experimental and simulated first-order
582 reversal curve measurements, the natural surface roughness of anti-
583 dots is at the origin of a parallel interaction field. These features
584 could be also present in our antidots.

585 An additional etching operation at the surface of the alumina
586 membranes might contribute to the reduction of the corrugated
587 profile of antidots. For instance, an appropriate ion-milling proce-
588 dure of antidots has led to a smoothing of a AAO surface.⁴⁶ As a
589 result, we could differentiate what is coming from the geometrical
590 roughness of antidots and what is coming from the spin orientation

at the edges of the nanopores. The next study will be focused on 591
this particular point. 592

As detailed in a previous study,²⁵ the relative proportions of 593
magnetic atoms deposited inside the nanopores vs those on the top 594
of membranes, namely, c_{Walls} and c_{Top} , respectively, are evaluated as 595
the form 596

$$c_{Top} = \frac{1 - (\pi/4)(d/p)^2}{S_{Total}}, \quad (1)$$

$$c_{Walls} = \frac{\pi dL/p^2}{S_{Total}}, \quad (2)$$

where $S_{Total} = 1 - \pi(d/2p)^2 + \pi dL/p^2$ and L is the penetration 598
length of the deposited multilayer along the inner pore wall. These 599
equations can be applied to calculate proportions of deposited 600
material inside the pores and on top for our antidots where d and 601
period p are known. 602

In the following, we discuss the c_{walls} and c_{top} values, as well as 603
 p , d , and the ratios of coercivity, exchange bias and anisotropy 604
between antidots (AAO) and continuous multilayer (CML) 605
obtained from our present study and those reported in literature 606
(Table III). We have selected planar and perpendicular systems 607
with unbiased and biased magnetic layers. For the calculation, a 608
penetration depth of $L = 30$ nm was assumed since this value has 609
been suggested for sputtered multilayers by Sousa *et al.*¹ and also 610
reported by Ref. 47, as well as found in our work from an analysis 611
performed by polarized x-ray absorption spectroscopy.²⁵ In addition, 612
the magnetic field during magnetic measurements is applied 613
following the easy axis except Refs. 18 and 19 and in our study, and 614
the operating temperature is also indicated in Table III. 615

In the references listed in Table III, a well-defined hexagonal 616
network of nanopores is observed as in the case of our antidots, 617
and the values of d and p are relatively close to ones presented in 618
that study. FC procedures from 300 K have been only performed 619
for Refs. 12 and 13 for low temperature measurements (10 K). For 620
Ref. 11, annealing has been performed at a temperature higher than 621
RT (230 °C) for 30 min in a magnetic field of 1.5 kOe to promote 622
the exchange bias effects. And a magnetic field of 250 Oe was 623
applied perpendicularly to the film plane during depositing to 624
induce the exchange bias effects in Ref. 24. Concerning Ref. 12, two 625
different continuous substrates have been used, Si(001) and Al₂O₃ 626
(0001); only the results for the latter substrate are presented here. 627
For the case of Si(001), similar tendency was observed. For the 628
other cited references, Si,^{9,13,15,16,24} SiO₂,^{11,21} and glass¹⁷⁻¹⁹ contin- 629
uous substrates were used. 630

For the whole of references cited in Table III, anodic alumina 631
membrane templates were prepared by a two-step anodization 632
process by using oxalic^{9,10,16-19,48,49} or sulfuric^{11-13,15} acid, expect 633
for Ref. 21 where nanoporous anodized titania (TiO₂) templates 634
were fabricated by two-stage anodization of Ti film in ammonium 635
fluoride solution in ethylene glycol. For Ref. 9, at very low tempera- 636
ture (2 K), the exchange bias is lowered for the continuous substrate 637
in the (2-250) K range of operating temperature as listed in 638
Table III; nevertheless, the result is the reverse for higher tempera- 639
tures. Here, the values are weak for both substrates 640

TABLE III. Comparison of structural characteristics and magnetic properties of antidots (named AAO), as well as continuous stack (named CML), reported in the literature and analyzed in this present study. Mentioned biased (B) and unbiased (UB) systems are separated in planar (\rightarrow) and perpendicular (\uparrow) magnetic anisotropy. Listed informations of antidots are as follows: the multilayer system (thickness in nm), pore diameter d and period p (in nm), calculated proportions of material deposited on the walls (c_{walls} , %) and the substrate surface (c_{top} , %) in % from the model developed in the Ref. 25, operating temperature, coercive field, exchange bias and anisotropy field of the antidot, and the associated values of the continuous structure (CML) are indicated in parentheses. The direction of the magnetic field is applied in the easy direction except Refs. 18 and 19 and in our study. The sign “-” means a planar magnetic anisotropy and a sign “+” a PMA, the * in the anisotropy field meaning that we have calculated this value from the area between perpendicular and planar published M(H) loops. In colors (blue, red, and green) are corresponding to cases where absolute values of bias and coercivity (anisotropy field) are increased (decreased) for antidots. These latter cases are discussed in the paper. Here, “No” means the absence of measurements.

Systems	d (nm)/ p (nm)	c_{walls} (%) / c_{top} (%)	T (K)	H_C (Oe)	H_{EXC} (Oe)	H_A (kOe)	Reference
UB \rightarrow , NiFe(18)	54/105	36.8/63.2	300	120(2)	...	$\approx^* - 0.11(-4.90)$	48
UB \rightarrow , NiFe(80)	55/105	37.5/62.5	300	60(14)	...	No	49
UB \rightarrow , Ni(20)	30/103	22.2/77.8	300	180(130)	...	$* - 0.61(-0.94)$	50
UB \rightarrow , Co(20)	30/103	22.2/77.8	300	280(38)	...	$* - 1.26(-1.44)$	50
B \rightarrow , FeMn(15)/Co(20)/FeMn(15)	50/80	51.5/48.5	2	514(98)	-97(-92)	No	9
B \rightarrow , (NiFe(20)/FeMn(15)) ₁₀	60/120	32.8/67.2	300	30(11)	-114(-65)	No	10
B \rightarrow , IrMn(8)/CoFe(10)	45/60	67.9/32.1	300	502(29)	-227(-148)	No	11
B \rightarrow , Co(1.5)/NiO(5) FC	40/90	35.5/65.5	10	320(4084)	-150(-1977)	No	12
B \rightarrow , Co(8)/NiO(5) FC	40/90	35.5/65.5	10	2418(2275)	-2081(-1539)	$* - 4.62(-7.95)$	12
B \rightarrow , Co(8)/NiO(1) FC	50/110	31.7/68.3	10	3977(1717)	-3386(-999)	No	13
B \rightarrow , Co(8)/NiO(20) FC	50/110	31.7/68.3	10	2506(1409)	-2042(-1293)	No	13
B \rightarrow , CoO(1.9)/Co(1.4) ₇ FC	64/107	41.7/58.3	60	441(70)	-146(-41)	No	14
B \rightarrow , Pt(5)/Co(0.6)/FeMn(2)	40.9/98.4	31.5/68.5	5	2517(2820)	3(2)	-2.14(+0.41)	Our study
B \rightarrow , Pt(5)/Co(0.6)/FeMn(3.5)	55.8/148.3	21.2/78.8	5	2625(3226)	-127(-58)	-2.13(-5.17)	Our study
B \rightarrow , Pt(5)/Co(0.6)/FeMn(3.5) FC	55.8/148.3	21.2/78.8	5	2614(5034)	-299(-3239)	No	Our study
B \rightarrow , Pt(5)/Co(0.6)/FeMn(5.5)	42.7/99.9	32.0/68.0	5	3338(2501)	-496(-39)	-4.83(-5.14)	Our study
UB \uparrow , (Co(0.5)/Pt(2)) ₅	30/60	49.4/50.6	300	1350(140)	...	$\approx^* + 3.00(+5.53)$	15
UB \uparrow , CoCrPt(10)	55.7/105	37.9/62.1	300	361(151)	...	$\approx^* + 0.63(+5.47)$	16
UB \uparrow , TbCo(30)	75/105	51.7/48.3	300	5000(2000)	...	$* + 3.04(+12.43)$	17
UB \uparrow , DyFe(30)	45/105	31.0/69.0	300	$\approx 926(545)$...	$* + 1.54(-11.18)$	18,19
UB \uparrow , (Co(0.5)/Pd(1)) ₅	35/140	15.0/85.0	5	3500(2000)	...	No	20
UB \uparrow , Pt(5)/Co(0.5)	56.4/101.7	40.4/59.6	5	1418(1194)	...	+1.48(+2.16)	Our study
B \uparrow , (Co(0.5)/Pt(0.5)) ₅ /IrMn(15)	40/100	30.1/69.9	300	50(200)	-566(-333)	No	24
B \uparrow , (Co(0.5)/Pd(1)) ₅ /CoFe(0.8)/IrMn(6)	50/100	37.2/62.8	300	1306(562)	-241(-194)	No	21
B \uparrow , IrMn(6)/CoFe(0.8)/(Pd(1)/Co(0.5)) ₅	50/100	37.2/62.8	300	1525(966)	-18(-13)	No	21
B \uparrow , IrMn(6)/CoFe(0.8)/(Pd(1)/Co(0.5)) ₅	30/100	23.3/76.7	300	1263(505)	-190(-179)	No	22
B \uparrow , Pt(5)/Co(0.6)/FeMn(5.5) FC	42.7/99.9	32.0/68.0	5	3335(4400)	+779(+2157)	+1.93(+4.18)	Our study

641 ($-H_{EXC} < 100$ Oe) and the trilayer defined by FeMn/Co/FeMn is a
642 structure more complex than a simple bilayer one with Co and
643 FeMn. For Refs. 10 and 11, other results are published with similar
644 tendency (both coercivity and bias fields higher for antidots)
645 merged in Table III. In these previous works, $(\text{NiFe}_X/\text{Co}_{150})_{10}$ ¹⁰
646 where X varies in the (40–60–80–100) nm range and for different
647 hole diameters [(2–5.5) nm] and pore diameter in the (7–45) nm
648 range¹¹ have been studied.

649 Now we discuss the behaviors of coercivity, exchange bias, and
650 anisotropy as a function of employed substrate (antidots vs contin-
651 uous) for a given easy axis (planar or perpendicular) and for (biased
652 or unbiased) structures.

653 **(1) Magnetic anisotropy.** By using the formula for the anisotropy
654 field ($H_A = 2 \int_0^{H_{\max}} dH \cdot [M_Z(H_Z^{\text{mean}}) - M_X(H_X)]$), for planar and
655 perpendicular magnetic fields (H_{\max} designating the field where
656 the magnetization is saturated), H_A is calculated from the mag-
657 netic loops published in Refs. 12, 15, 16, 17, 18, 19, 48, and 50, as
658 indicated by “*” in the anisotropy field column in Table III. For
659 Refs. 15, 16, and 48, even if the applied magnetic field is not effi-
660 cient for getting the saturation, an extrapolation of the magnetic
661 hysteresis is applied for the calculation of H_A . We systematically
662 found $|H_A(\text{antidots})| < |H_A(\text{CML})|$ for the different published
663 references as well as for our results, except for the $X = 2$ nm mul-
664 tilayer (as highlighted in green color in Table III). For a given
665 easy axis (planar for Refs. 12, 48, 50 and our results or perpendic-
666 ular for Refs. 15–19 and our results) and for a continuous stack, by
667 introducing a perforated network, additional opposite (perpendic-
668 ular/planar) magnetic moments are induced in the valley of anti-
669 dots such that the total anisotropy field is reduced for the
670 discontinuous sample. For instance, for the case of Ni antidot
671 arrays,⁵¹ the continuous structure, as well as the antidot ones for
672 d in the (35–80) nm range, behave as a planar magnetic anisotropy
673 ($H_A < 0$). More d is less $-H_A$ for antidot is recorded due to
674 the increase in the out-of-plane magnetic moments in the valley
675 of nanoholes. A PMA is only favored for the largest hole diame-
676 ters ($d > 80$ nm), and the anisotropy sign changes (from negative
677 to positive value inducing out-of-plane magnetic anisotropy). The
678 same tendency is observed in Refs. 18, 19, and 51 for DyFe(30)
679 and Ni, respectively. Concerning the $X = 2$ nm stack, the situa-
680 tion is the reverse for the substrates: a weak PMA (+0.41 kOe) is
681 obtained for the continuous sample antidot whereas a moderate
682 in-plane magnetic anisotropy (–2.14 kOe) is achieved for the
683 antidot. Indeed, the anisotropy field changes sign from positive to
684 negative by using an antidot substrate. This particular feature
685 explains the strongest absolute magnetic anisotropy field for the
686 antidot larger than the one of the continuous stacks. Moreover,
687 the field cooling procedure re-orientates the magnetization in the
688 perpendicular direction for the $X = 5.5$ nm multilayer for both
689 substrates, leading to positive H_A first reported for biased perpen-
690 dicular antidots in the literature.

691 **(2) Coercive fields.** Concerning unbiased antidots systems, the coer-
692 civity is systematically enhanced by employing the antidot as a
693 substrate. The applied magnetic field is in the direction of the easy
694 magnetization (planar for Refs 48–50 and perpendicular magnetic
695 anisotropy for Refs. 15–20), and holes act as pinning centers of
696 domain wall displacement, specially at the edges of the pores

during magnetization reversal. This feature is largely admitted in
the literature.^{11–17,20,21,23,40,43,48,50} For the biased systems, results
seem more contrasted at a first sight. $H_C(\text{AAO}) > H_C(\text{CML})$ is
measured for most of Refs. 9, 10, 11, 12, 13, 14, 21, and 22. Here,
the applied magnetic field is applied in the easy direction of the
magnetization. Nevertheless, for our samples with $X = (2 - 3.5)$
nm measured after a ZFC procedure, and possibly the 3.5 nm
samples after a FC one, the perpendicular applied magnetic field
being now a hard axis for the antidots. In the same way, FC mea-
surements show similar features for systems with low ferromag-
netic thicknesses [(1.5–3) nm Co for Ref. 12] with, in particular,
an asymmetric hysteresis loop for the sheet samples and a
two-step magnetization reversal process in the antidot arrays for 3
nm Co, similarly to our study.⁴⁴ Concerning Ref. 24,
 $H_C(\text{AAO}) < H_C(\text{CML})$ is also observed. For both samples in the
previous reference, a perpendicular magnetic field has been used
during the deposition. Consequently, the nature of the easy axis
and the role of the magnetic field (for a FC-procedure or during
the disposition) have drastic influences on the amplitude of
the coercivity. A possible explanation is the three-dimensional
magnetization effect induced by the valley of nanoholes and the
magnetic field reinforcing the coercivity for the sheet sample
rather than for the discontinuous one. This might be the case for
our $X = 5.5$ nm samples after a FC procedure [$H_C(\text{AAO}) = 3335$
Oe $< H_C(\text{CML}) = 4400$ Oe]. Finally, for the antidot deposited
with the high antiferromagnetic thickness ($X = 5.5$ nm) and for
the ZFC procedure, even if the magnetic is planar for both
samples as indicated in Table III, coercivity is larger for the
antidot. Here, the antiferromagnetic coupling for both samples is
high such that the pinning effects around valleys of nanoholes
lead to larger H_C for the antidot compared to the continuous
structure.

697 **(3) Exchange bias fields.** The exchange bias is lowered for the
sheet sample compared to the antidot, expected the group in
Ref. 12 for $\text{Co}_{15}/\text{NiO}_{50}$ as seen in red color in Table III. Similar
features are checked for our multilayers ($X = 3.5$ and 5.5 nm).
All these measurements include a FC-procedure, indicating once
again the key role of the applied magnetic field on the arrange-
ment of the magnetic moments on the 3D-profile of antidots.
For Ref. 24, $H_C(\text{AAO}) < H_C(\text{CML})$ but $|H_{EXC}(\text{AAO})| > |H_{EXC}$
(CML)| whereas a magnetic field has been employed during the
deposition. This particular result seems to establish the predomi-
nant role of the magnetic field during the FC procedure on the
one during the deposition.

To our knowledge, there are no published results combining
variations of coercivity, bias as well as anisotropy as a function of
structural dimensions (as hole diameter). A noteworthy investiga-
tion, showing variations of H_C and K_{eff} as a function of d at RT in
20 nm-Ni antidot arrays thin film (where $p = 103$ nm), is found in
Ref. 51. For a magnetic field orientated in the easy direction of the
magnetization, $H_C(\text{AAO}) > H_C(\text{CML})$ is also found. We can also
note the behaviors of H_C and H_{EXC} as a function of d in CoO/Co
multilayer thin films (where $p = 107$ nm) in Ref. 14.

A discussion about the variation of the coercivity, exchange
bias, and the magnetic anisotropy for the whole of data published
in the literature (see Table III) is difficult due to the different

753 nature of systems, the different thicknesses of magnetic layers, and
754 the nature of the magnetic measurements (ZFC or FC, or magnetic
755 field applied during the deposition or post-deposition). An effort
756 could be done for a series of samples with, for instance, a fixed
757 stack (unique composition and same thicknesses) and by varying
758 only the hole diameter. From our part, a forthcoming paper will
759 detail magnetic properties of exchange-coupled Cu/Co/Cu trilayers
760 for operating temperature in the (5–400) K range and for different
761 d . Nevertheless, variations of the coercivity for biased planar (left-
762 bottom part) and perpendicular (top-right part) antidots as a func-
763 tion of the walls content c_{Walls} are plotted in Fig. 7. The data are
764 extracted from the literature and from our own results, as merged
765 in Table III. Here, the hole diameter d is comprised between 40
766 and 60 nm, even if p is varied between 60 and 150 nm. For these
767 studies, the magnetic field is applied in the *easy direction* of magne-
768 tization. A general tendency indicates an increase in the coercivity
769 when the fraction of atoms on the valley of antidots enhances. The
770 density of pinning sites imposed by the antidots pores leads to
771 strong coercivity at least for c_{Walls} in the (20–70)% range for biased
772 planar systems and the (30–40)% range for biased perpendicular
773 systems. A second reason at the origin of the increase of H_C is the
774 magnetization reversal more favorable via domain wall movement
775 (low wedge-to-wedge s value), as claimed by other studies.^{2,50–52}
776 And for highest c_{Walls} values (i.e., large hole diameter), it is
777 observed that the coercivity for antidots is drastically lowered when
778 d is enhanced, as in Refs. 15 and 51 for unbiased perpendicular
779 and planar multilayers, respectively, c_{Walls} reach 69% and 66% for
780 Refs. 15 and 51, respectively. The loss of the magnetic anisotropy
781 and the magnetization reversal coherent rotation^{50–52} constitute
782 two factors explaining the decrease in coercivity with c_{Walls} .

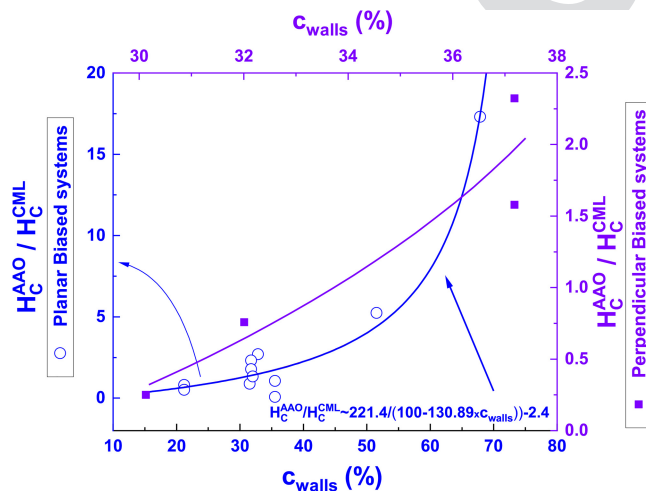
783 A second way to estimate the importance of wall fraction is to
784 take account the wedge-to-wedge distance between two consecutive

785 holes ($s = p - d$ as introduced in Table I). By using this previous
786 relation and replacing $d = p - s$ in Eq. (2), it arrives

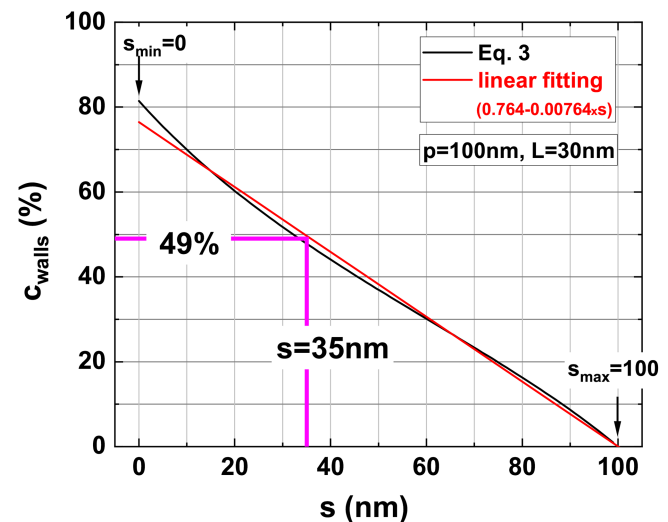
$$c_{Walls} = \frac{\pi(p-s)L/p^2}{1 - \pi\left(\frac{p-s}{2p}\right)^2 + \pi\frac{(p-s)L}{p^2}} \quad (3)$$

788 Here, $p = 100$ nm (as largely used in the literature),
789 $L = 30$ nm, and s is varied in the (0–100) nm. The s dependence of
790 c_{Walls} is given in Fig. 8. As expected, c_{Walls} decreases with s , a linear
791 fit leads to $c_{Walls} \approx 0.764 - 0.00764 \cdot s$ (where s is
792 expressed in nm). Here, the good quality of linear fitting is
793 observed for s in the (10–100) nm range, where typical dimensions
794 are used for the fabrication of antidots. As example, $s = 35$ nm (or
795 $d = 65$ nm currently used for antidots in the literature) leads to
796 $c_{Walls} = 49\%$ (see the vertical and horizontal lines in Fig. 8). This
797 model [Eq. (3)] can be easily used for a unique stack where only s
798 (or d) is varied (p being fixed), in order to quantify c_{Walls} .

799 In many reports,^{2,49–51,53–55} coercivity is assumed to vary as
800 $H_C \propto 1/(p-d) = 1/s$. Therefore, an increase in d (or a decrease
801 of s) leads to an enhancement of the coercivity. This corresponds to a
802 regime where the nanoholes are more or less disconnected from each
803 other, i.e., for high s or low c_{Walls} . In fact, the pinning effects become
804 more prominent when the magnetic atoms are mainly deposited
805 around the nanoholes. Consequently, a strong magnetic field is neces-
806 sary to overcome the pinning coupling. Then, from the linearity of s
807 and c_{Walls} , H_C can be rewriting as $H_C \approx 1/(100 - 130.89 \times c_{Walls})$.
808 In Fig. 7, $H_C^{AAO}/H_C^{CML} = 221.4/(100 - 130.89 \times c_{Walls}) - 2.4$ is
809 derived from a adjustment of data via our model, revealing its
810 validity.



784 FIG. 7. H_C^{AAO}/H_C^{CML} ratio vs calculated proportions of material deposited on the
785 walls (c_{Walls}) for biased antidots systems with planar (left-bottom part) and per-
786 pendicular (top-right part) magnetic anisotropy. The data are extracted from the
787 literature and are also corresponding to our present study (see Table III for addi-
788 tional information about the sample and the operating temperature).



789 FIG. 8. Calculated proportions of material deposited on the walls (c_{Walls}) vs the
790 wedge-to-wedge distance between two consecutive holes (s) from Eq. (3). Here,
791 $p = 100$ nm, $L = 30$ nm, and a linear adjustment is added for easily calculating
792 c_{Walls} starting from s .

811 A third way for analyzing the magnetic features is to consider
812 the filling factor, namely, the porosity (Po) defined by^{1,48,56}

$$Po = \frac{\pi(d/p)^2}{2\sqrt{3}}. \quad (4)$$

813 By replacing d with Po [from Eq. (4)], and using Eq. (2), c_{Walls}
815 reads

$$c_{Walls} = \frac{\pi L/p}{\left[\frac{2\sqrt{3}Po}{\pi}\right]^{-1/2} - \left[\frac{2\sqrt{3}Po}{\pi}\right]^{1/2} + \frac{\pi L}{p}}. \quad (5)$$

816 The Po dependence of c_{Walls} is plotted in Fig. 9 in the left-
818 bottom part where $p = 100$ and $L = 30$ nm. c_{Walls} is enhanced
819 when the porosity is increased as expected. In the (15–58)% range
820 of porosity, a linear fitting as $c_{Walls} \approx 0.2214 + 0.6588 \times Po$ might
821 be used for an accurate estimation of the atomic proportion in the
822 periphery of nanopores. As example, $Po = 40\%$ leads to
823 $c_{Walls} = 49\%$, corresponding to $s = 35$ nm (see the vertical line in
824 Fig. 9). Equation (5) can be easily used, for a unique stack where
825 only Po is varied (p fixed), in the aim to calculate c_{Walls} from Po .

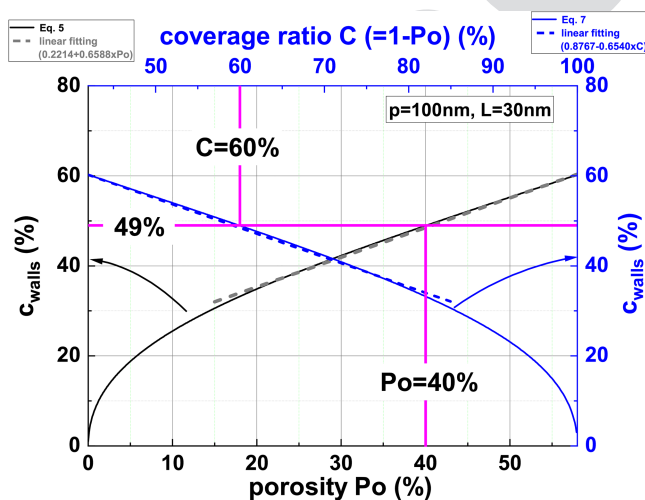
826 Finally, the coverage ratio C is defined as $C = 1 - Po$,^{14,52} i.e.,

$$C = 1 - \frac{\pi(d/p)^2}{2\sqrt{3}}. \quad (6)$$

828 As a consequence, Eq. (7) permits to express c_{Walls} as a func-
829 tion of C ,

$$c_{Walls} = \frac{\pi L/p}{\left[\frac{2\sqrt{3}(1-C)}{\pi}\right]^{-1/2} - \left[\frac{2\sqrt{3}(1-C)}{\pi}\right]^{1/2} + \frac{\pi L}{p}}. \quad (7)$$

830



831 **FIG. 9.** Calculated proportions of material deposited on the walls (c_{Walls}) vs the
832 porosity Po from Eq. (5) in the bottom-left part, and vs the coverage ratio C
833 ($= 1 - Po$) in the top-right-part. Here, $p = 100$ nm, $L = 30$ nm, and linear
834 adjustments are added for easily calculating c_{Walls} starting from Po or C .

The top-right part of Fig. 9 gives the variation of c_{Walls} with C .
 c_{Walls} decreases when C is enhanced, similarly to $c_{Walls}(s)$ (see
Fig. 8). Higher values of C correspond to less material deposited
around the holes. The value of 49% for c_{Walls} from the previous
example corresponds to a coverage ratio $C = 60\%$ (or $Po = 40\%$,
see the vertical line in Fig. 9). In the (42–85)% range of C , a
linear fit as $c_{Walls} \approx 0.8767 - 0.6540 \times C$ might be used for an accurate
estimation of the atomic proportion in the periphery of nanopores.
Here, we check that the slopes of linear fittings appearing in Fig. 9
are opposite due to the simple relation $C = 1 - Po$.

By merging Eqs. (2), (3), (5), and (7), and considering an
antidot network where p is fixed, and $L = 30$ nm, we are able to
express c_{Walls} as a function of d , s , Po , and C , respectively. The mag-
netic properties of the sample (coercivity, exchange bias, anisotropy,
etc.) might be discussed in the light of variation of these
structural parameters. It would be interesting to possibly use these
expressions for magnetic studies devoted to antidots.

V. CONCLUSION

From intensive extraordinary Hall effects performed at 5 K, biased
 $\text{Ta}(5 \text{ nm})/\text{Pt}(5 \text{ nm})/\text{Co}(0.6 \text{ nm})/\text{FeMn}(X)/\text{Ta}(5 \text{ nm})$ stacks
employing two types of substrates (antidots vs Si/SiO_2) for X in the
(0–5.5) nm range reveal either planar magnetic anisotropy for ZFC
measurements and $X \neq 0$, or perpendicular magnetic anisotropy for
ZFC data for $X = 0$ samples (both multilayer sheet and antidot)
and for $X = 2$ nm (only sheet sample), and by using a
FC-procedure (with a maximum temperature around Néel temper-
ature of FeMn) for $X = 5.5$ nm. From perpendicular magnetic
fields data, more X is more both $|H_{EXC}|$ and H_C enhanced for the
series of antidots and sheet samples (accompanied by a weak
decrease for the largest X thickness for the large regime of X), as
expected for ferromagnetic/antiferromagnetic exchange-coupled
nanostructures. As discussed from our results as well as in pub-
lished data in the literature, we believe that $H_C(\text{AAO}) > H_C(\text{CML})$,
 $|H_{EXC}(\text{AAO})| > |H_{EXC}(\text{CML})|$, and $|H_A(\text{AAO})| < |H_A(\text{CML})|$ for
ZFC measurements with magnetic fields in the *easy* direction of
the magnetization performed on continuous and antidots samples
behaving similar signs of the magnetic anisotropy. For magnetic
fields in the *hard* direction of the magnetization and/or FC proce-
dures with efficient maximum temperature ($\approx T_b$ and/or $\approx T_N$)
performed on the discontinuous sample containing moderate thick-
nesses ($X < 5$ nm), these inequalities of coercivity and exchange
bias might be in the opposite way due to the 3D-profile of nanopores.
In addition, we have expressed the structural parameters, such as
the wedge-to-wedge distance (s), the porosity (Po), and the coverage
ratio (C) as a function of proportion of atoms deposited in the
nanopores. The geometry of antidots, as well as the magnetic and
thermal history of the nanodevice, tunes the magnetic properties of
magnetic antidots. This can lead to antidots which is an interesting
possibility for synthesizing and controlling skyrmions.

ACKNOWLEDGMENTS

F. Fettar thanks Alexis Wartelle for a critical reading of this
manuscript.

884 AUTHOR DECLARATIONS

885 Conflict of Interest

886 The authors have no conflicts to disclose.

887 Author Contributions

888 **F. Fettar:** Conceptualization (lead); Data curation (lead); Formal
889 analysis (lead); Investigation (lead); Methodology (lead); Resources
890 (equal); Software (equal); Supervision (lead); Validation (lead);
891 Writing – original draft (lead); Writing – review & editing (sup-
892 porting). **L. Cagnon:** Resources (equal); Visualization (equal).
893 **D. Barral:** Investigation (equal); Methodology (equal); Resources
894 (equal). **P. David:** Investigation (equal); Methodology (equal);
895 Resources (equal). **L. Naudin:** Writing – review & editing (equal).
896 **F. Blondelle:** Investigation (equal); Methodology (equal);
897 Resources (equal). **F. Gay:** Investigation (equal); Methodology
898 (equal); Resources (equal).

899 DATA AVAILABILITY

900 The data that support the findings of this study are available
901 from the corresponding author upon reasonable request.

902 REFERENCES

903 ¹C. T. Sousa, D. C. Leitao, M. P. Proenca, J. Ventura, A. M. Pereira, and
904 J. P. Araujo, “Nanoporous alumina as templates for multifunctional applica-
905 tions,” *Appl. Phys. Rev.* **1**(3), 031102 (2014).
906 ²C. Castán-Guerrero, J. Herrero-Albillos, J. Bartolomé, F. Bartolomé,
907 L. A. Rodríguez, C. Magén, F. Kronast, P. Gawronski, O. Chubykalo-Fesenko,
908 K. J. Merazzo, P. Vavassori, P. Strichovanec, J. Sesé, and L. M. García, “Magnetic
909 antidot to dot crossover in Co and Py nanopatterned thin films,” *Phys. Rev. B*
910 **89**(14), 144405 (2014).
911 ³M. Kovylina, M. Erekhinsky, R. Morales, J. E. Villegas, I. K. Schuller,
912 A. Labarta, and X. Batlle, “Tuning exchange bias in Ni/FeF₂ heterostructures
913 using antidot arrays,” *Appl. Phys. Lett.* **95**(15), 152507 (2009).
914 ⁴S. Saha, M. Zelent, S. Finizio, M. Mruczkiewicz, S. Tacchi, A. K. Suszka,
915 S. Wintz, N. S. Bingham, J. Raabe, M. Krawczyk, and L. J. Heyderman,
916 “Formation of Néel-type skyrmions in an antidot lattice with perpendicular mag-
917 netic anisotropy,” *Phys. Rev. B* **100**(14), 144435 (2019).
918 ⁵R. V. Verba, D. Navas, A. Hierro-Rodríguez, S. A. Bunyaev, B. A. Ivanov,
919 K. Y. Guslienko, and G. N. Kakazei, “Overcoming the limits of vortex formation
920 in magnetic nanodots by coupling to antidot matrix,” *Phys. Rev. Appl.* **10**(3),
921 031002 (2018).
922 ⁶D. Navas, R. V. Verba, A. Hierro-Rodríguez, S. A. Bunyaev, X. Zhou,
923 A. O. Adeyeye, O. V. Dobrovolskiy, B. A. Ivanov, K. Y. Guslienko, and
924 G. N. Kakazei, “Route to form skyrmions in soft magnetic films,” *APL Mater.*
925 **7**(8), 081114 (2019).
926 ⁷R. V. Verba, D. Navas, S. A. Bunyaev, A. Hierro-Rodríguez, K. Y. Guslienko,
927 B. A. Ivanov, and G. N. Kakazei, “Helicity of magnetic vortices and skyrmions in
928 soft ferromagnetic nanodots and films biased by stray radial fields,” *Phys. Rev. B*
929 **101**(6), 064429 (2020).
930 ⁸H. Masuda and K. Fukuda, “Ordered metal nanohole arrays made by a
931 two-step replication of honeycomb structures of anodic alumina,” *Science*
932 **268**(5216), 1466–1468 (1995).
933 ⁹C. Jiang, D. Xue, X. Fan, D. Guo, and Q. Liu, “Anomalous positive exchange
934 bias in nanostructured FeMn/Co/FeMn networks,” *Nanotechnology* **18**(33),
935 335703 (2007).
936 ¹⁰N. N. Phuoc, S. L. Lim, F. Xu, Y. G. Ma, and C. K. Ong, “Enhancement of
937 exchange bias and ferromagnetic resonance frequency by using multilayer
938 antidot arrays,” *J. Appl. Phys.* **104**(9), 093708 (2008).

¹¹N. N. Shams, M. Tofizur Rahman, and C.-H. Lai, “Defect mediated tuning of
exchange bias in IrMn/CoFe nanostructure,” *J. Appl. Phys.* **105**(7), 07D722 (2009).
¹²W. J. Gong, W. J. Yu, W. Liu, S. Guo, S. Ma, J. N. Feng, B. Li, and
Z. D. Zhang, “Exchange bias and its thermal stability in ferromagnetic/antiferro-
magnetic antidot arrays,” *Appl. Phys. Lett.* **101**(1), 012407 (2012).
¹³W. J. Gong, W. Liu, J. N. Feng, D. S. Kim, C. J. Choi, and Z. D. Zhang, “Effect
of antiferromagnetic layer thickness on exchange bias, training effect, and mag-
netotransport properties in ferromagnetic/antiferromagnetic antidot arrays,”
J. Appl. Phys. **115**(13), 133909 (2014).
¹⁴M. Salaheldeen, A. Nafady, A. M. Abu-Dief, R. Díaz Crespo, M. Paz
Fernández-García, J. Pedro Andrés, R. López Antón, J. A. Blanco, and
P. Álvarez-Alonso, “Enhancement of exchange bias and perpendicular magnetic
anisotropy in CoO/Co multilayer thin films by tuning the alumina template
nanohole size,” *Nanomaterials* **12**(15), 2544 (2022).
¹⁵M. T. Rahman, N. N. Shams, C. H. Lai, J. Fidler, and D. Suess, “Co/Pt perpen-
dicular antidot arrays with engineered feature size and magnetic properties fabri-
cated on anodic aluminum oxide templates,” *Phys. Rev. B* **81**(1), 014418 (2010).
¹⁶D. Navas, F. Ilievski, and C. A. Ross, “CoCrPt antidot arrays with perpendicular
magnetic anisotropy made on anodic alumina templates,” *J. Appl. Phys.* **105**(11),
113921 (2009).
¹⁷N. A. Kulesh, M. Vázquez, V. N. Lepalovskij, and V. O. Vas'kovskiy, “Antidot
patterned single and bilayer thin films based on ferrimagnetic Tb–Co alloy with
perpendicular magnetic anisotropy,” *Nanotechnology* **29**(6), 065301 (2018).
¹⁸M. Salaheldeen, V. Vega, A. Ibabe, M. Jaafar, A. Asenjo, A. Fernandez, and
V. Prida, “Tailoring of perpendicular magnetic anisotropy in Dy₁₃Fe₈₇ thin films
with hexagonal antidot lattice nanostructure,” *Nanomaterials* **8**(4), 227 (2018).
¹⁹M. Salaheldeen, V. Vega, R. Caballero-Flores, V. M. Prida, and A. Fernández,
“Influence of nanoholes array geometrical parameters on magnetic properties of
Dy–Fe antidot thin films,” *Nanotechnology* **30**(45), 455703 (2019).
²⁰T. Ngoc Anh Nguyen, J. Kasiuk, W.-B. W. Julia Fedotova, J. Przewoźnik,
C. Kapusta, O. Kupreeva, S. Lazarouk, T. Thanh Hai Cao, T. Thanh Thuy
Nguyen, H. Manh Dinh, K. Tung Do, T. Huong Nguyen, H. K. Vu, D. Lam Vu,
and J. Åkerman, “Correlation of magnetic and magnetoresistive properties of
nanoporous Co/Pd thin multilayers fabricated on anodized TiO₂ templates,” *Sci.
Rep.* **10**(1), 10838 (2020).
²¹T. N. Anh Nguyen, J. Fedotova, J. Kasiuk, W.-B. Wu, J. Przewoźnik,
C. Kapusta, O. Kupreeva, S. Lazarouk, T. H. Thuy Trinh, K. Tung Do, H. Manh
Do, D. Lam Vu, and J. Åkerman, “Enhanced perpendicular exchange bias in
Co/Pd antidot arrays,” *J. Electron. Mater.* **48**(3), 1492–1497 (2018).
²²W.-B. W. Julia Kasiuk, T. Ngoc Anh Nguyen, J. Fedotova, J. Przewoźnik,
C. Kapusta, O. Kupreeva, S. Lazarouk, K. Tung Do, T. Huong Nguyen, H. K. Vu,
D. Lam Vu, and J. Åkerman, “Complex magnetic ordering in nanoporous
[Co/Pd]₅₀–IrMn multilayers with perpendicular magnetic anisotropy and its
impact on magnetization reversal and magnetoresistance,” *Phys. Chem. Chem.
Phys.* **22**(6), 3661–3674 (2020).
²³W.-B. W. Julia Kasiuk, T. Ngoc Anh Nguyen, J. Przewoźnik, J. Fedotova,
C. Kapusta, O. Kupreeva, S. Lazarouk, K. Tung Do, T. Huong Nguyen, H. K. Vu,
H. Linh Pham, D. Lam Vu, and J. Åkerman, “Influence of interfacial magnetic
ordering and field-cooling effect on perpendicular exchange bias and magnetoresis-
tance in nanoporous IrMn/[Co/Pd] films,” *J. Appl. Phys.* **127**(22), 223904 (2020).
²⁴Z. Shi, X. X. Fan, P. He, S. M. Zhou, H. N. Hu, M. Yang, and J. Du, “Exchange
bias of perpendicularly magnetized [Co/Pt]₃/IrMn multilayer on porous anod-
ized alumina,” *J. Appl. Phys.* **113**(17), 17D722 (2013).
²⁵H. Garad, S. Usmani, D. Barral, P. David, L. Cagnon, D. Testemale,
D. Mannix, F. Fettar, O. Proux, A. Rosa, O. Mathon, and S. Pascarelli, “Influence
of the pore diameter in Cu/Co/Cu antidots: A XANES study,” *Phys. Rev. Mater.*
2(6), 066001 (2018).
²⁶A. Clavijo, O. Caballero-Calero, and M. Martín-González, “Revisiting anodic
alumina templates: From fabrication to applications,” *Nanoscale* **13**(4),
2227–2265 (2021).
²⁷I. Dobosz, “Influence of the anodization conditions and chemical treatment
on the formation of alumina membranes with defined pore diameters,” *J. Porous
Mater.* **28**(4), 1011–1022 (2021).

- 1002 ²⁸R. A. Khan, H. T. Nembach, M. Ali, J. M. Shaw, C. H. Marrows, and
1003 T. A. Moore, "Magnetic domain texture and the Dzyaloshinskii-Moriya interac-
1004 tion in Pt/Co/IrMn and Pt/Co/FeMn thin films with perpendicular exchange
1005 bias," *Phys. Rev. B* **98**(6), 064413 (2018).
- 1006 ²⁹R. Jungblut, R. Coehoorn, M. T. Johnson, J. aan de Stegge, and A. Reinders,
1007 "Orientational dependence of the exchange biasing in
1008 molecular-beam-epitaxy-grown Ni₈₀Fe₂₀/Fe₅₀Mn₅₀ bilayers (invited)," *J. Appl.*
1009 *Phys.* **75**(10), 6659–6664 (1994).
- 1010 ³⁰C.-P. Li, I. V. Roshchin, X. Batlle, M. Viret, F. Ott, and I. K. Schuller,
1011 "Fabrication and structural characterization of highly ordered sub-100-nm
1012 planar magnetic nanodot arrays over 1 cm² coverage area," *J. Appl. Phys.* **100**(7),
1013 074318 (2006).
- 1014 ³¹L. Zaraska, G. D. Sulka, and M. Jaskuła, "Anodic alumina membranes with
1015 defined pore diameters and thicknesses obtained by adjusting the anodizing
1016 duration and pore opening/widening time," *J. Solid State Electrochem.* **15**-
1017 (11-12), 2427–2436 (2011).
- 1018 ³²N. Nagaosa, J. Sinova, S. Onoda, A. H. MacDonald, and N. P. Ong,
1019 "Anomalous Hall effect," *Rev. Mod. Phys.* **82**(2), 1539–1592 (2010).
- 1020 ³³J. Nogués and I. K. Schuller, "Exchange bias," *J. Magn. Magn. Mater.* **192**(2),
1021 203–232 (1999).
- 1022 ³⁴H. Sang, Y. W. Du, and C. L. Chien, "Exchange coupling in Fe₅₀Mn₅₀/
1023 Ni₈₁Fe₁₉ bilayer: Dependence on antiferromagnetic layer thickness," *J. Appl.*
1024 *Phys.* **85**(8), 4931–4933 (1999).
- 1025 ³⁵H. Saglam, W. Zhang, M. B. Jungfleisch, J. Sklenar, J. E. Pearson,
1026 J. B. Ketterson, and A. Hoffmann, "Spin transport through the metallic antiferro-
1027 magnet FeMn," *Phys. Rev. B* **94**(14), 140412 (2016).
- 1028 ³⁶Y. Dahmane, C. Arm, S. Auffret, U. Ebels, B. Rodmacq, and B. Dieny,
1029 "Oscillatory behavior of perpendicular magnetic anisotropy in Pt/Co/Al(Ox)
1030 films as a function of al thickness," *Appl. Phys. Lett.* **95**(22), 222514 (2009).
- 1031 ³⁷S. Okamoto, N. Kikuchi, O. Kitakami, T. Miyazaki, Y. Shimada, and
1032 K. Fukamichi, "Chemical-order-dependent magnetic anisotropy and exchange stiff-
1033 ness constant of FePt (001) epitaxial films," *Phys. Rev. B* **66**(2), 024413 (2002).
- 1034 ³⁸J. Gräfe, F. Haering, T. Tietze, P. Audehm, M. Weigand, U. Wiedwald,
1035 P. Ziemann, P. Gawronski, G. Schütz, and E. J. Goering, "Perpendicular magnet-
1036 isation from in-plane fields in nano-scaled antidot lattices," *Nanotechnology*
1037 **26**(22), 225203 (2015).
- 1038 ³⁹A. Fraile Rodríguez, A. C. Basaran, R. Morales, M. Kovylna, J. Llobet,
1039 X. Borrísé, M. A. Marcus, A. Scholl, I. K. Schuller, X. Batlle, and A. Labarta,
1040 "Manipulation of competing ferromagnetic and antiferromagnetic domains in
1041 exchange-biased nanostructures," *Phys. Rev. B* **92**(17), 174417 (2015).
- 1042 ⁴⁰D. R. Saldanha, D. A. Dugato, T. J. A. Mori, N. F. Daudt, L. S. Dorneles, and
1043 J. C. Denardin, "Tailoring the magnetic and magneto-transport properties of
1044 Pd/Co multilayers and pseudo-spin valve antidots," *J. Phys. D: Appl. Phys.*
1045 **51**(39), 395001 (2018).
- 1046 ⁴¹S. Michea, S. Oyarzún, S. Vidal, and J. C. Denardin, "Enhanced Hall effect in
1047 Co/Pd multilayered nanodomes with perpendicular anisotropy," *AIP Adv.* **7**(5),
1048 056310 (2017).
- 1049 ⁴²X. J. Honglyou Ju, D. E. McCready, and K. M. Krishnan, "Interface structure
1050 and perpendicular exchange bias in (Co/Pt)_n/FeMn multilayers," *J. Appl. Phys.* **1050**
1051 **98**(11), 116101 (2005).
- 1052 ⁴³M. Tofizur Rahman, N. N. Shams, and C.-H. Lai, "A large-area mesoporous
1053 array of magnetic nanostructure with perpendicular anisotropy integrated on Si
1054 wafers," *Nanotechnology* **19**(32), 325302 (2008).
- 1055 ⁴⁴F. Fettar, L. Cagnon, and N. Rougemaille, "Three-dimensional magnetization
1056 profile and multiaxes exchange bias in Co antidot arrays," *Appl. Phys. Lett.* **1056**
1057 **97**(19), 192502 (2010).
- 1058 ⁴⁵F. Béron, K. R. Pirota, V. Vega, V. M. Prida, A. Fernández, B. Hernando, and
1059 M. Knobel, "An effective method to probe local magnetostatic properties in a
1060 nanometric FePd antidot array," *New J. Phys.* **13**(1), 013035 (2011).
- 1061 ⁴⁶D. C. Leitao, J. Ventura, C. T. Sousa, J. M. Teixeira, J. B. Sousa, M. Jaafar,
1062 A. Asenjo, M. Vazquez, J. M. De Teresa, and J. P. Araujo, "Tailoring the physical
1063 properties of thin nanohole arrays grown on flat anodic aluminum oxide tem-
1064 plates," *Nanotechnology* **23**(42), 425701 (2012).
- 1065 ⁴⁷Y. Lei and W.-K. Chim, "Shape and size control of regularly arrayed nanodots
1066 fabricated using ultrathin alumina masks," *Chem. Mater.* **17**(3), 580–585 (2005).
- 1067 ⁴⁸K. J. Merazzo, D. C. Leitao, E. Jiménez, J. P. Araujo, J. Camarero, R. P. del
1068 Real, A. Asenjo, and M. Vázquez, "Geometry-dependent magnetization reversal
1069 mechanism in ordered Py antidot arrays," *J. Phys. D: Appl. Phys.* **44**(50), 505001
1070 (2011).
- 1071 ⁴⁹K. R. Pirota, P. Prieto, A. M. J. Neto, J. M. Sanz, M. Knobel, and M. Vazquez,
1072 "Coercive field behavior of permalloy antidot arrays based on self-assembled
1073 template fabrication," *J. Magn. Magn. Mater.* **320**(14), e235–e238 (2008).
- 1074 ⁵⁰M. Salaheldeen, V. Vega, A. Fernández, and V. M. Prida, "Anomalous
1075 in-plane coercivity behaviour in hexagonal arrangements of ferromagnetic
1076 antidot thin films," *J. Magn. Magn. Mater.* **491**, 165572 (2019).
- 1077 ⁵¹M. Salaheldeen, M. Méndez, V. Vega, A. Fernández, and V. M. Prida, "Tuning
1078 nanohole sizes in Ni hexagonal antidot arrays: Large perpendicular magnetic
1079 anisotropy for spintronic applications," *ACS Appl. Nano Mater.* **2**(4), 1866–1875
1080 (2019).
- 1081 ⁵²M. Krupinski, D. Mitin, A. Zarzycki, A. Szkudlarek, M. Giersig, M. Albrecht,
1082 and M. Marszałek, "Magnetic transition from dot to antidot regime in large area
1083 Co/Pd nanopatterned arrays with perpendicular magnetization,"
1084 *Nanotechnology* **28**(8), 085302 (2017).
- 1085 ⁵³D. Navas, M. Hernández-Vélez, M. Vázquez, W. Lee, and K. Nielsch,
1086 "Ordered Ni nanohole arrays with engineered geometrical aspects and magnetic
1087 anisotropy," *Appl. Phys. Lett.* **90**(19), 192501 (2007).
- 1088 ⁵⁴J. Gräfe, G. Schütz, and E. J. Goering, "Coercivity scaling in antidot lattices in
1089 Fe, Ni, and NiFe thin films," *J. Magn. Magn. Mater.* **419**, 517–520 (2016).
- 1090 ⁵⁵P. Prieto, K. R. Pirota, M. Vazquez, and J. M. Sanz, "Fabrication and magnetic
1091 characterization of permalloy antidot arrays," *Phys. Status Solidi (A)* **205**(2),
1092 363–367 (2007).
- 1093 ⁵⁶K. J. Merazzo, R. P. del Real, A. Asenjo, and M. Vázquez, "Dependence of
1094 magnetization process on thickness of permalloy antidot arrays," *J. Appl. Phys.* **1094**
1095 **109**(7), 07B906 (2011).